Study and Development of Pulse-shape Discrimination Firmware for Background Mitigation in the DEAP Experiment

by

Simon T. Norman-Hobbs

A THESIS SUBMITTED IN PARTIAL FULFILMENT OF
THE REQUIREMENTS FOR THE DEGREE OF

Bachelor of Science

in

The Faculty of Science

(Physics)

The University of British Columbia

April 2016

Abstract

Study and Development of Pulse-shape Discrimination Firmware for Background
Mitigation in the DEAP Experiment

by

Simon T. Norman-Hobbs

Bachelor of Science in Physics

University of British Columbia

DEAP-3600 is a particle detector looking for weakly interacting massive particles (WIMPs) as a source of dark matter using a 3600 kg atmospheric argon target. Incident particles colliding with the argon should produce excited dimers which decay releasing scintillation light. Different particle characteristics determine the proportion of excited states of the dimers produced, and events can be characterized by the timing of the light released. Atmospheric argon produces ~ 1 Hz/kg of ^{39}Ar $\beta-$decay. To reduce the background rate from $\beta-$decay a trigger is introduced in order to remove a proportion of these backgrounds through pulse shape discrimination techniques. It is necessary that possible WIMP events and rare background events are not miscategorized as $\beta-$decays, so careful calibration is essential so as not to reduce the sensitivity of the experiment. This project describes the design and development of this trigger algorithm followed by thorough testing and characterization of the trigger's behaviour. The trigger is now operational and has been installed in the detector. Studies of the trigger's behaviour indicate its functionality. A study of the efficiency in the turn-on zones is also presented.

Contents

List of Figures

List of Tables

Table of Symbols

$^1\Sigma_{\mathbf{u}}$ Singlet state eximer with time constant τ_1.

$^3\Sigma_{\mathbf{u}}$ Triplet state eximer with time constant τ_3.

AARF Acrylic Reflector and Fiber Optics, a system of LED light injection used for detector calibration.

ASUM Analog Sum, an analog sum of the signals from 12 PMTs passed to the DTM from each of the SCBs.

ASUMSUM A digital sum of the 22 analog sums from the SCBs, used in the trigger logic.

AV Acrylic Vessel, central container for the liquid argon target.

$\mathbf{\Lambda CDM}$ Lambda-Cold Dark Matter, the standard cosmological model which postulates that our universe's expansion is dominated by a cosmological constant (Λ) and cold dark matter CDM.

CMB Cosmic Microwave Background.

CP Charge Parity, CP-symmetry there should be no change if a particle were interchanged with its antiparticle and then the left and right handed particles were reversed Axion dark matter arises as a proposed solution to observed CP violations in QCD.

DAQ Data Aquisition, the system of digitizers and backend computers recording and saving data to disk.

DEAP Dark Matter Experiment using Argon Pulse-shape discrimination.

DEAP-1 Prototype detector for DEAP-3600 with a 7 kg target mass of liquid Ar.

DEAP-3600 Dark matter detector with a 3600 kg target mass of liquid Ar.

DM Dark Matter.

DTM Digital Trigger Module, control board for the DAQ.

erf Gaussian error function.

FPGA Field Programmable Gate Array.

Fprompt Fraction of Prompt Light, the integrated charge in a short window divided by the charge from an entire event. Used in PSD to determine incident particle type.

KK Kaluza-Klein extra-dimensional particle states.

LED Light Emitting Diode, used in AARF calibration system.

LET Linear Energy Transfer, the energy deposited by an incident particle per unit length (dE/dx).

LKP Lightest Kaluza-Klein Particle, a possible CDM candidate.

MACHO MAssive Compact Halo Object, conjectured nonluminous bodies of stellar mass or above.

MOND Modified Newtonian Dynamics.

m.w.e Meters of Water Equivalent, attenuation level of surface and extraterrestrial background sources.

PE Photo Electron, used as a unit of charge from an event calculated by pulse counting on the digitizers.

PLL Phase Lock Loop, clock frequency multiplier that hold the relative phase of the input output clocks fixed.

PMMA Polymethyl methacrylate, acrylic used in the DEAP light guides.

PMT Photomultiplier Tube.

PPG Pattern Pulse Generator, injects electronic pulses which cause the trigger to fire.

PSD Pulse Shape Discrimination.

QCD Quantum Chromodynamics.

ROOT C++ data analysis library set developed by CERN.

SCB Signal Conditioning Board, core of the front end system, which prepares PMT signals to be digitized.

SM Standard model of particle physics.

SNOLAB Underground clean room facility near Sudbury, Ontario where DEAP-3600 and DEAP-1 are located. The facility is 2 km underground with a 6010 m.w.e overburden.

SUSY Supersymmetry, a popular extension to the standard model.

TPB 1,1,4,4-tetraphenyl-1,3-butadiene, the wavelength shifter used in DEAP, re-emits at 425 nm.

V1720 CAEN V1720 12-bit, 8-channel waveform digitizing modules with a 250 MS/s sampling rate.

V1740 CAEN V1740 12-bit, 8-channel waveform digitizing modules with a 62.5 MS/s sampling rate.

VUV Vacuum Ultraviolet light, light with a wavelength between 10 and 200 nm.

WIMP Weakly Interacting Massive Particle.

WMAP Wilkinson Microwave Anisotropy Probe.

ZLE Zero Length Encoding, a storage optimization routine in the V1720 digitizers. Discards an event if a threshold of total charge is not meet.

Acknowledgments

It is an honour for me to thank all those that helped make this project come to fruition. I would like to thank my supervisor Fabrice Retiere and all the members of the DEAP collaboration, especially Ben Smith, Thomas Linder, Pierre-André Armundez, and Yair Linn. If it were not for their constant help this would not have been possible. I would like to thank my parents Maureen Norman and my father Philip Hobbs for their encouragement, support, prayers, and proof-reading. I'd additionally like to thank Chris Mann, Birgit Rogalla, and Alexandra Merkouriou for challenging me and making such excellent study partners over my undergraduate career.

"Don't sweat the petty things, and don't pet the sweaty things."

— George Carlin

Chapter 1

Introduction

DEAP-3600 is a direct dark matter detector that is currently in the last stages of development. DEAP-3600 uses liquid argon as a scintillation target looking for incoming weakly interacting dark matter particles. Projected to be the first detector sensitive enough to probe the constrained minimum supersymmetric model's (cMSSM) neutrilino mass and cross-section predictions, DEAP will either give evidence in support of this theory or set a new limit on the mass and cross-section for particle dark matter.

The triggering system of DEAP-3600 is a complex system that controls the data recording electronics. Due to high rates of β-decay in atmospheric argon, the trigger must preform dynamic event rejection in such a way as to maximize the sensitivity of the detector while reducing this background. A robust, reliable and well understood trigger is a crucial component of high sensitivity particle detectors and DEAP-3600 is no exception. This project is the development and study of the triggering system. The design and motivation is covered as well as the development process and testing. Testing of the triggers efficiency and behaviour in rejecting and accepting events is covered.

This project is comprised of two primary parts: firmware development and testing and trigger analysis. The trigger analysis looks at data taken using light injection to characterize the behaviour of the triggering system when installed on the detector.

Chapter 2

Dark Matter: Theory and Detection

It is well established that the majority of the matter in our universe remains undetected. The currently accepted cosmological model (known as the standard cosmological model or ΛCDM) states that the dominant make up of matter in the universe is non-relativistic (cold) and non-baryonic (dark) [23]. In this chapter I summarize the argument for cold dark matter (CDM), several CDM candidates, and some of the prominent past and on going experiments for determination of the cause of CDM.

2.1 Missing Mass & the Case for Dark Matter

2.1.1 Missing Mass Observations

The term dark matter (DM) as a way of referring to a form of non-luminous matter was first used by Kapteyn [27] as a future direction for his studies of stellar dynamics in the disk of the Milky Way. Kapteyn predicted that the distribution of any non-luminous, or dark, matter could be determined by observing the rotation curves of stars in the Milky Way. The issue of missing mass was first observed by Zwicky in 1933 while measuring the red-shifts of galaxies in the Coma cluster (Abell 1656) [47] (English translation: [48]). His observations found velocities in excess of 2000 km/s for the cluster, which has a luminous mass on the order of 1.6×10^{45} g. If the system can be assumed to be in a mechanically

steady state, then the virial theorem predicts that:

$$\bar{\epsilon}_k = -\frac{1}{2}\bar{\epsilon}_p, \tag{2.1}$$

($\bar{\epsilon}_k$ and $\bar{\epsilon}_p$ are the kinetic and potential energies). Using Eq. (2.1) and the observed mass of the luminous matter, the average velocity for galaxies in the cluster would be ~ 80 km/s. This disparity in density (measured by Zwicky to be at least 400 times the density inferred from the stars alone) is the origin of the missing mass problem and the first observational evidence for dark matter.

Following Zwicky's work, little was done to investigate dark matter until galactic dynamics studies of the Andromeda galaxy were done by Rubin and Ford in 1970 [40]. They found that the rotation curves did not fit with the virial theorem for the visible matter in the same manner as was observed by Zwicky, reporting a H1 to total mass ratio of between 4 and 8 percent.

According to Newtonian mechanics the rotation of an orbit should follow:

$$v(r) = \sqrt{\frac{GM(r)}{r}}. \tag{2.2}$$

Crucially, outside the majority of the system's mass, any test mass should have an orbital velocity that drops proportional to $1/\sqrt{r}$; however, this is not observed. The angular velocity of objects around the galactic center remains essentially constant as see in Fig. 2.1. This observation indicates an increasing mass/luminosity ratio with radius [39] where previously little matter was believed to exist. Observations of a disparity between luminous matter and a system's rotation curve have been seen in essentially every study for many different galaxies, groups, and clusters with similar results, for example NGC 300 & M33 [22], NGC 4038/39 [41], and M81 [39]. Two conclusions can be drawn from this information: 1) Our theory of gravity is incorrect at these scales, or 2) A large amount of non-relativistic dark matter (CDM) is not being accounted for and extends well beyond the baryonic mass in these systems.
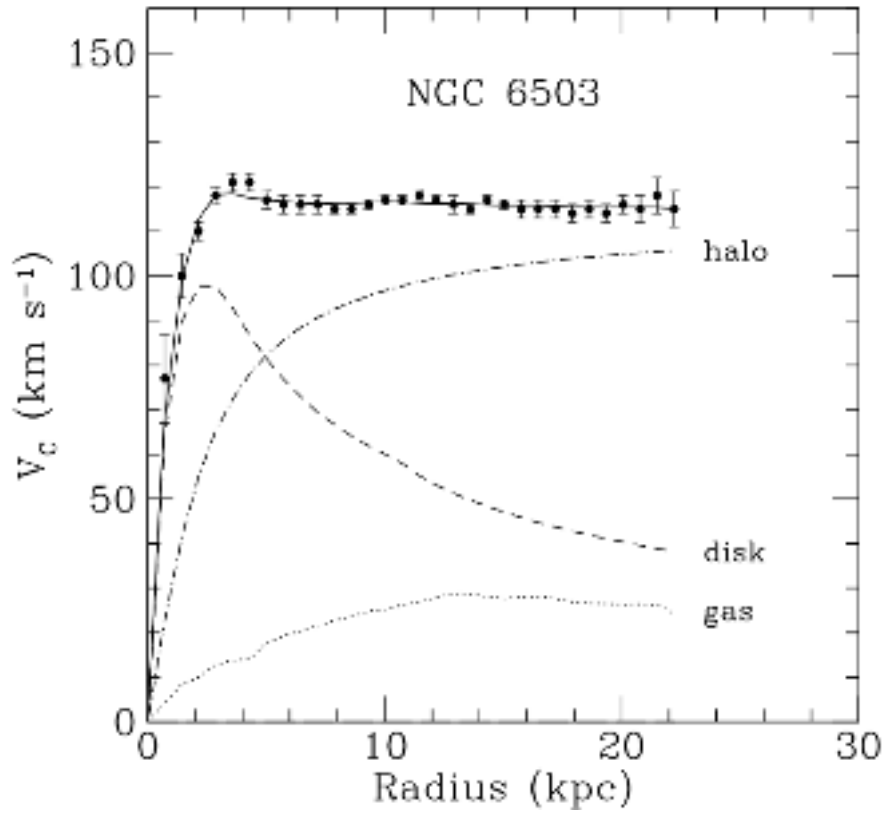
Figure 2.1: Rotation curve fit to NGC 6503. The disparity between the measured rotation curve (points), the stellar mass in the disk (dashed line), and the interstellar gas (dotted line) is attributed to an isothermal dark halo (dash-dot line). The sum of these components are the solid fit line [6]. The measured rotation curve is essentially constant with increasing radius past 2 kpc. If the mass were distributed like the visible component, the rotation curve would drop off $\propto 1/\sqrt{r}$ at large radii.

2.1.1.1 MOND & the Bullet Cluster

Modified Newtonian Mechanics (MOND) postulates that the Newtonian $1/r^2$ relation for gravitating bodies only holds for forces and distances similar to those in the solar system, but that the decline in force with distance is less for weaker forces [32]. MOND has been used to reproduce the rotation velocities of spiral galaxies without the necessity of additional mass beyond that of the observed baryons and a small neutrino component [33]. Work done by Clowe, Gonzalez, and Markevitch in 2004 on mass reconstruction of the interacting cluster 1E0657-558 (the Bullet Cluster) showed that even in a MOND construction, dark matter of greater mass than the total baryonic contribution was necessary to explain their observations [15].

The Bullet Cluster is an interacting group which has just undergone initial in-fall and pass-through of two different clusters. An x-ray emitting gas has been stripped and separated from the main and sub clusters which are interacting due to the ram-pressure during collision, shown in false colour in Fig. 2.2. The galaxies themselves are mainly unaffected in the collision, leaving their gaseous components lagging behind [44]. As the majority of the visible mass in the cluster is found in the gaseous halo, the Bullet Cluster allows for a definitive test of MOND.

If MOND is correct and all of the mass is of baryonic or neutrino origins, then the mass peak should match the x-ray emission peak (which contains the bulk of the clusters mass). On the other hand, if weakly-interacting CDM is the vast majority of the mass, then the peak will be centred around the galactic centres which are separated from the gaseous halos. Mass measurements were done using weak lensing effects, which put the mass peak near the galactic halos. A total mass on the order of $10^{14} M_\odot$ was found, which is in close agreement to the velocity dispersion measurements made for early-type galaxies by Barrena et al. (2002) [5]. Even under the MOND model, a non-baryonic mass greater than the that of the baryons is needed, the very problem it was formulated to solve. Thus current formulations of MOND appear to be excluded.
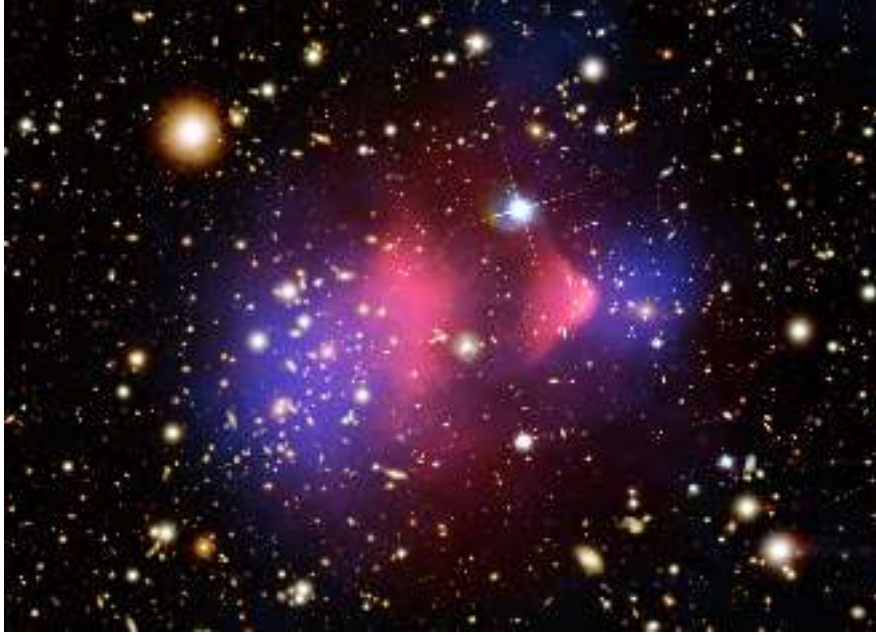
Figure 2.2: False colour composite image of the interacting cluster 1E0657-558 (the Bullet Cluster). X-ray emissions from the hot interstellar gas (red) accounts for $\sim 80\%$ of the baryonic matter in the cluster. The gas has been stripped from the galactic cores in the collision. The mass in the cluster (blue), measured from micro-lensing studies, is shown to be separated from the x-ray emitting gas, occurring instead around the galactic centres. The mass distribution from the study of this cluster is one of the most definitive arguments for weakly interacting particle dark matter. Composite Credit: x-ray: NASA/CXC/CfA/ M.Markevitch et al.; Lensing Map: NASA/STScI; ESO WFI; Magellan/U.Arizona/ D.Clowe et al. Optical: NASA/STScI; Magellan/U.Arizona/D.Clowe et al. [15]

2.1.2 Cosmic Microwave Background & ΛCDM

Possibly the most convincing argument for the existence of cold dark matter comes from studies of the cosmic microwave background radiation (CMB). A widely accepted model for the state of our universe is the ΛCDM, or standard, cosmological model. ΛCDM is fully characterized by six parameters: the age of the universe (t_0), the current Hubble parameter (H_0), density fluctuations (Δ_R^2), the energy densities of baryons (ϵ_b) and cold dark matter (ϵ_{CDM}), and the cosmological constant (Λ). The model assumes the universe is spatially flat and is dominated by a cosmological constant (Λ) and cold dark matter (CDM). Extensive studies of the cosmic microwave background radiation (CMB) by WMAP [23] have found that the model is an adequate fit to the observable CMB, large scale structure data,

Table 2.1: Six parameter ΛCDM fit to the WMAP nine year data [23].

Parameter	Symbol	WMAP Data
Age of Universe (Gyr)	t_0	13.74 ± 0.11
Hubble Parameter (H$_0$ = 100h kms^{-1}Mpc^{-1})	H_0	70.0 ± 2.2
Baryon Density/Critical Density	$\Omega_b h^2$	0.0463 ± 0.0024
Cold Dark Matter Density/Critical Density	$\Omega_c h^2$	0.233 ± 0.023
Dark Energy Density/Critical Density	$\Omega_\Lambda h^2$	0.721 ± 0.025
Curvature Perturbations, k$_0$ = 0.002 Mpc^{-1}	$10^9 \Delta_R^2$	2.41 ± 0.10

age of globular clusters, observed expansion rates, neutron abundance, and supernovae observations [23].

The parameter values of the WMAP study are given in Table. 2.1. The values of interest to the present study are the DM to baryon proportions. The quantity Ω_x for a species x is defined in terms of its energy density (ρ_x) and the critical energy density (i.e. the density at which curvature is zero) of the universe (ρ_c) as given by:

$$\rho_c \equiv \frac{3H^2}{8\pi G} \tag{2.3}$$

$$\Omega_x \equiv \frac{\rho_x}{\rho_c} \tag{2.4}$$

These values are important because the expansion rate of the universe is given by the Friedmann equation for scale factor a, curvature k, and Hubble parameter H:

$$\sum_x \Omega_x - 1 = \frac{k}{H^2 a^2}. \tag{2.5}$$

The curvature value k is one of three values: 0, -1 or 1. The average energy density of the universe determines the curvature, if the density is equal to the critical-density then the universe is spatially flat (k = 0). A subcritical-density universe is negatively curved (k = -1), and a supercritical-density universe is positively curved (k = 1).

The findings of WMAP put tight constraints on the characteristics of dark matter. The observations require that there exist particles that interact gravitationally but are chargeless and non-baryonic. Additionally, these particles must be stable or long-lived enough to have survived since the early universe. From the rotation curves discussed
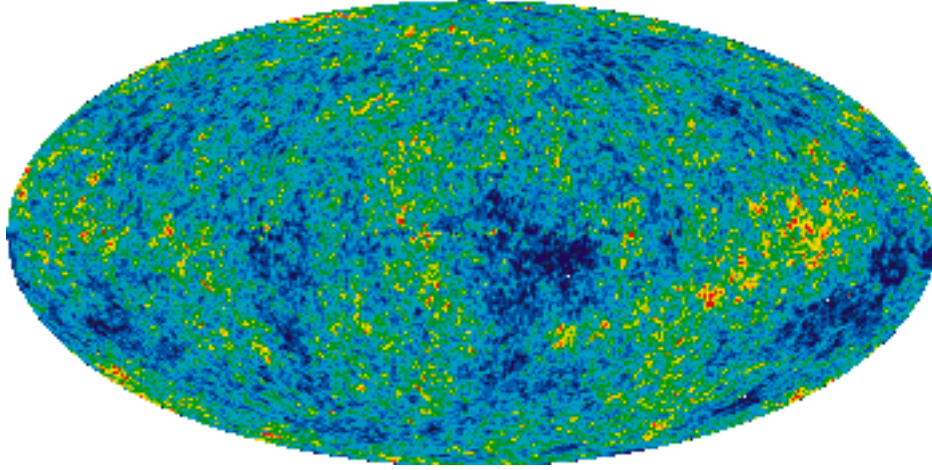
Figure 2.3: All-sky temperature profile from the nine year WMAP data release with the Milky Way removed and multipole corrected for our peculiar velocity [23]. Fluctuations are shown as color differences corresponding to growth areas of large structures. The temperature range of these fluctuations are within $\pm$ 200 μK. Credit: NASA / WMAP Science Team

above, we infer that dark matter is the dominant constituent of large structures. From the observed clumping it is expected that dark matter must be have been non-relativistic, or cold, at the point of structure formation [23].

As our galaxy exhibits a rotation curve similar to those of other spiral galaxies, we can conclude that the Milky Way contains a typical amount of DM distributed in a similar manner to others [43]. Therefore, due to dark matter's pervasiveness in our galaxy and the fact that it has yet to be detected, it is assumed to not interact via either the electromagnetic or strong force. Dark matter does, of course, interact gravitationally, and weak interactions have not been ruled out [46].

The evidence for a form of cold and non-baryonic dark matter is compelling and well motivated; however it has yet to be detected. Several viable candidates have been introduced and are briefly discussed below. It is important to note that dark matter need not all be of the same species, several may contribute.

It must be added that there are known species of nonluminous matter that contribute to the observed phenomena. Massive compact halo objects or MACHOs are baryonic masses that were conjectured to exist in galactic halos but to be too faint to be currently observable. Their existence in galactic halos would contribute to the increasing mass-

luminosity relations observed in galactic rotation curves [7]. However being baryonic, MACHOs cannot explain all the WMAP observations.

Another known species of dark matter is the Standard Model (SM) neutrino. The neutrino is a lepton, thus non-baryonic, and does not interact electromagnetically or via the strong force. The neutrino, however, is known to have a very small mass, thus is unlikely to make-up a significant portion of dark matter [7]. A larger issue is that neutrinos are relativistic (or hot) and would not explain large scale structure formation [7]. In short, the ideal particle that fits the requirements for DM while still being detectable is the family of theorized weakly interacting massive particles (WIMPs).

2.1.3 Relic Density

In an expanding universe such as that predicted by the ΛCDM model, a particle species in the early universe would remain in local thermodynamic equilibrium until the expansion rate of the universe (H(t)) exceeded the reaction rate per particle (Γ) defined as:

$$\Gamma \equiv n\sigma v \tag{2.6}$$

with the particles total annihilation cross section σ, velocity v, and number density n. Roughly at this equilibrium point, the particle is said to have decoupled or frozen out. Following the argument presented by Bertone, Hooper, and Silk (2004) [7], the number density of a species x after freeze-out (n_x) is determined from the Boltzmann equation and can thus be expressed by:

$$\frac{dn}{dt} + 3Hn = -\langle\sigma n\rangle\left(n^2 - (n^{eq})^2\right), \tag{2.7}$$

where the number density at thermal equilibrium is n^{eq} [7]. For particles in the non-relativistic limit such as WIMPs, this can be expressed for particle mass m at temperature T with g degrees of freedom as given by:

$$n^{eq} = g\left(\frac{mT}{2\pi}\right)^{3/2} e^{-m/T}. \tag{2.8}$$

Expanding $\langle \sigma v \rangle$ in powers of v^2, in terms of constants a and b expressed in GeV^{-2}, gives:

$$\langle \sigma v \rangle = a + b \langle v^2 \rangle \frac{T}{m} + O(\langle v^4 \rangle). \tag{2.9}$$

The general relic density for a particle species x can then be expressed in the non-relativistic, low temperature limit as:

$$\Omega_x h^2 \approx \frac{1.07^9 GeV^{-1}}{M_{PI}} \frac{m}{T_F \sqrt{g_*}} \frac{1}{a + 3b\frac{T_F}{m}}, \tag{2.10}$$

with g_* as the number of relativistic degrees of freedom evaluated at the freeze-out temperature (T_F) for a particle mass m. h is the dimensionless Hubble parameter, $h \equiv H_0/100$ km s^{-1} Mpc^{-1}. An order-of-magnitude approximation to Eq. (2.10) is often useful and is given by:

$$\Omega_x h^2 \approx \frac{3 \times 10^{-27} \text{ cm}^3 \text{ s}^{-1}}{\langle \sigma v \rangle} \approx \frac{m n_x}{\rho_c}. \tag{2.11}$$

A viable WIMP candidate should have a relic density that is constrained near that predicted by WMAP, which serves as a useful sanity check for a suggested theory.

2.2 WIMP Candidates

The Standard Model of particle physics (SM) is known to be an incomplete theory. For one example, it does not yet include neutrino oscillations [46]. There are numerous theorized extensions to the SM that include possible WIMPs including axions, WIMPzillas, neutralinos, sterile neutrinos, Kaluza-Klein states, and many others [7]. The leading candidate categories are discussed in the following.

2.2.1 Extra Dimensional States

The inclusion of extra spatial dimensions as a way to unify gravity and the electromagnetic forces was introduced mainly through the work of Kaluza in 1921 [26] with his classical extensions to general relativity followed by the inclusion of quantum theory by Klein in 1926 [28]. Kaluza-Klein (KK) states (standing waves) exist as a series (or tower) of different

masses determined by their mode number (n) and the radius of the spacial dimension (R) given by the series (in natural units):

$$m_n = \frac{n}{R}. \tag{2.12}$$

Each state in this series has the same quantum number, color, and charge. The first state is the lightest KK particle (LKP) and is predicted to have an annihilation cross section of $\sigma v \approx \frac{0.6\text{pb}}{m^2_{B(1)}[TeV]}$ which is large enough to be within the possible sensitivity of tonne scale detectors such as DEAP-3600 [46][7].

2.2.2   Axions

Charge-parity (CP) conservation is observed in quantum chromodynamics (QCD). This is an issue as there exists in the QCD Lagrangian a CP violating term; this disconnect between the theory of QCD and experimental results is known as the strong CP problem [46]. Introducing a scalar field to the problem (the Peccei-Quinn mechanism) is a credible scheme to preserve CP [46]. This theory predicts the existence of axions, pseudo Nambu-Goldstone bosons that arise from this solution.

Laboratory studies, stellar evolution, and observations of supernova 1987A have constrained the axion mass to less than 10^{-2} eV. Axions are expected to be extremely weakly interacting with ordinary particles, and thus the above derivation of relic density cannot be used and their distribution is not well understood. It is however, possible to meet all the constraints of particle dark matter within a range of possible axion characteristics [7].

2.2.3   Supersymmetric Particles

The supersymmetric theory (SUSY) states that for every SM particle there exists a superpartner (or sparticle), which differs from its counterpart only by 1/2 spin. Thus there would be a symmetry between fermions and force carrying bosons. By this theory there exists a fermion and boson for every particle type. SUSY predicts several possible DM candidates including the gravitino (graviton superpartner), the axino (axion superpartner), sneutrinos [21] (superpartner of SM neutrinos), and the neutralinos which are the four Majorana

fermionic mass states formed from the superpartners of the B and W_3 gauge bosons and the neutral Higgs bosons [46]. The first neutralino is the lightest supersymmetric particle; this would cause it to be stable and thus explain its survival since the big bang. The neutralino has a mass between 10 and 10,000 GeV, is weakly interacting, electrically neutral, and stable. Therefore the neuralino is a naturally emerging CDM candidate from minimal supersymmetric theories [35].

Although the neutralino has been the most investigated SUSY candidate, there exists an equally viable candidate the axino, which is the superparter to the axion. If axions are found to exist, then axinos would be a viable WIMP candidate [7].

2.3 Detecting WIMPs

There are several on going experiments that are searching for dark matter. These experiments fall into one of two categories: direct and indirect detection.

Indirect detection experiments look for annihilations of WIMPs in areas where the density is expected to be high, such as in the sun or the galactic center. Examples of these experiments are the cosmic neutrino detectors IceCube/AMANDA [1], and ANTARES [3], as well as the cosmic ray detectors EGRET [17], PAMELA/ATIC [20].

The second class of experiments is direct detection, of which DEAP is one. Direct detection methods look for interactions of DM particles from our galaxy's halo with Earth based sensors. Detectors are based on measuring charge (ionization), light (scintillation), or heat/sound (phonons) due to possible WIMP scattering event. DEAP relies on a single phase scintillation-based detection method that is discussed in Chapter 3. A diagram showing a few of the on going and planned experiments with their respective signal types are shown in Fig. 2.4.

2.3.1 Recoil and Cross Sections

Direct detection methods look for WIMP-like collisions or recoils as a way of determining the interaction cross section and mass of the particle under several assumptions about our
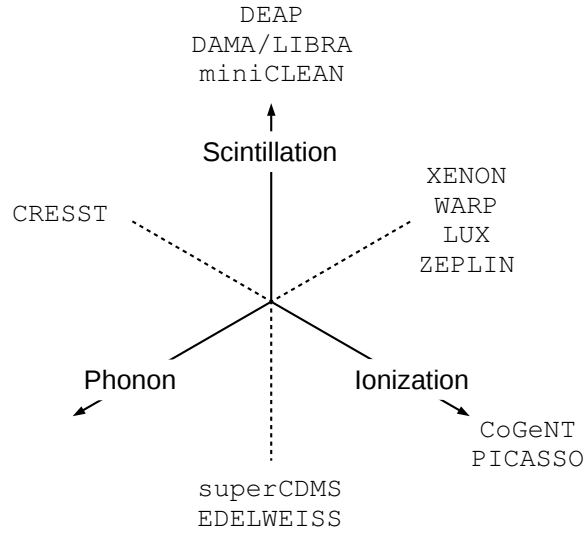
Figure 2.4: Diagram of the detection method used for a selection of the largest and most sensitive direct detection experiments. Several experiments combine signal types in their design. The DEAP-3600 design is a single phase argon scintillation detector.

galaxy's DM halo. The halo properties and expected WIMP induced recoils are outlined following the arguments given in Ref. [42] & [25].

With the application of Fermi's Golden Rule, the momentum transfer (q) dependant WIMP-nucleon scattering cross section ($\sigma(q)$) can be separated into two distinct parts: a momentum dependent form factor (F), and the zero momentum cross section (σ_0):

$$\frac{d\sigma(q)}{dq^2} = \frac{\sigma_0 F^2(q)}{4\mu_A^2 v^2}. \tag{2.13}$$

Here μ_A is the reduced mass for a WIMP mass M_χ and the target nuclei mass M_A:

$$\mu_A \equiv \frac{M_\chi M_A}{M_\chi + M_A}; \tag{2.14}$$

v is the velocity of the WIMP with respect to the nuclei. The cross section in the form given by Eq. (2.13) generally depends on if the WIMP couples to the spin of the target nucleus, or whether it is spin-independent and couples to all nucleons. The spin independent term
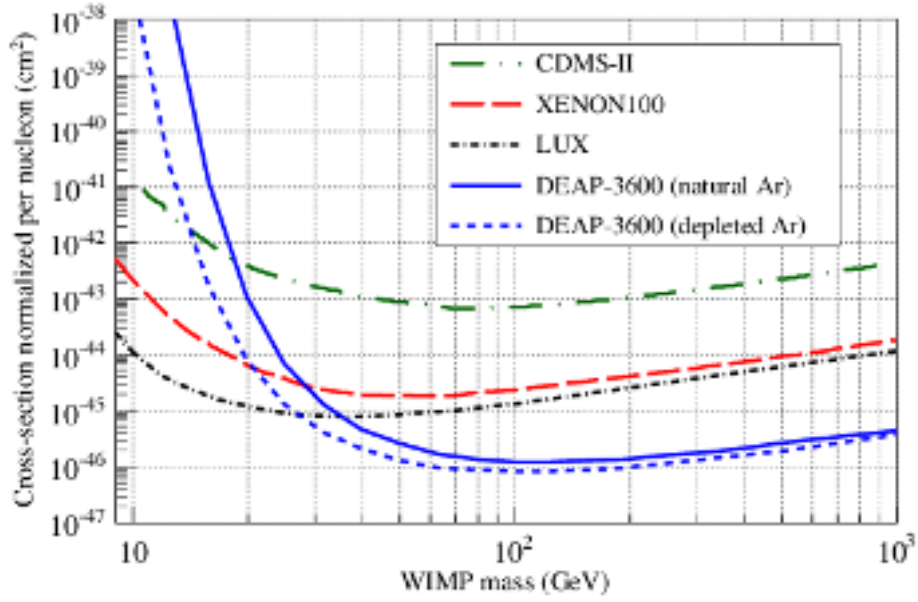
Figure 2.5: Current and projected limitations for the WIMP spin independent cross section as a function of mass. Due to its large size and high sensitivity, DEAP-3600 is anticipated to either detect or set a new lower bound for the ~ 100 GeV WIMP. Image source: [18].

of σ_0 is:

$$\sigma_{0,\mathrm{SI}} \equiv \sigma_{\mathrm{SI}} \frac{\mu_A^2}{\mu_n^2} A^2, \tag{2.15}$$

assuming that the coupling between neutrons and protons is similar. As spin-dependent interactions can only occur for a target nucleus with net spin, this term will vanish for target nuclei with even numbers of neutrons and protons such as the ^{40}Ar used in DEAP [42].

Current experimental limits on the WIMP spin-independent cross section have been set by the LUX experiment [31]. Current limits for mass and cross section are shown in Fig. 2.5 [18]. DEAP-3600 is projected to improve the current WIMP cross section lower limit by a factor of over 20 for 100 GeV mass WIMPs to a lower limit of 5.7×10^{-47}cm^2 [18] [12].

Chapter 3

DEAP

Dark matter **E**xperiment with liquid **A**rgon **P**ulse shape discrimination (DEAP) is an argon nuclei based noble liquid direct dark matter detection project designed to detect WIMP induced scintillation. In this chapter the detection process that DEAP uses is described as well as the detector's construction.

3.1 Scintillation

3.1.1 Noble Gas Scintillators

Scintillation is a light emitting interaction that occurs in certain materials known as scintillators. Incident radiation or particles that deposit energy in the scintillator cause the release of scintillation light. In liquid noble gases, when a nuclei is excited or ionized, they can form strong bonds with a ground state atom to form either an ionized or excited dimer state known as excimers [34]. These excimers are metastable and will radiatively decay. A diagram for a particle interaction producing scintillation light in argon is shown in Fig. 3.1.

Noble liquids are attractive medium choices in particle detectors due to their relatively low price, high light yield, scalability, and self-shielding ability. Of the noble liquids, neon, argon, krypton, and xenon have potential for use and have been used in other WIMP detectors such as LUX [31] and XENON [4]. Argon was chosen for a combination of reasons
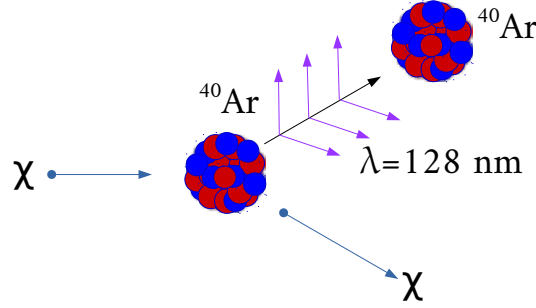
Figure 3.1: DEAP senses particle interactions through the release of ultraviolet light caused by the nuclear or electronic recoil of the argon nuclei.

Table 3.1: Properties of the noble gases [29]. Note prices are approximate and vary based on source and purity levels.

Property	He	Ne	Ar	Kr	Xe	Rn
Atomic Number	2	10	18	36	54	86
Atmospheric ppm	5	15.4	9400	1	$\frac{1}{20}$	10^{-15}
Cost per kg (CAD\$)	52.00	330.00	5.00	330.00	1200.00	-
Melting Point T_m (K)	-	24.6	83.8	115.8	161.4	202.0
Boiling Point T_b (K)	4.22	27.07	87.29	119.92	165.10	211.3

especially its high light yield, potential for single stage detection (see Section 3.1.2), and low cost [9] [18] [30].

Argon excimer formation occurs when an argon atom in atomic state $^3P_1$ or $^3P_2$ bonds with one in the $^1S_0$, or ground, state. There are therefore, two possible spin configurations for a dimer pair: a singlet state, $^1\Sigma_u(^3P_1 + {}^1S_0)$, or a triplet state, $^3\Sigma_u(^3P_2 + {}^1S_0)$ [34]. Both configurations are metastable and will decay releasing 128 nm vacuum ultraviolet light (VUV) as depicted in Fig. 3.2. There is no long lasting chemical change to the argon after an interaction.

Eximers can be formed through one of two mechanisms: direct excitation or ionization. Excitation occurs when one of the $^3P_1$ or $^3P_2$ atomic states forms a strong bond to a ground state atom which then radiatively decays [24]:

$$Ar^* + Ar \rightarrow Ar_2^*$$

$$Ar_2^* \rightarrow 2Ar + h\nu.$$

(3.1)

If an ion is produced, it must first recombine with a free electron and (non-radiatively)
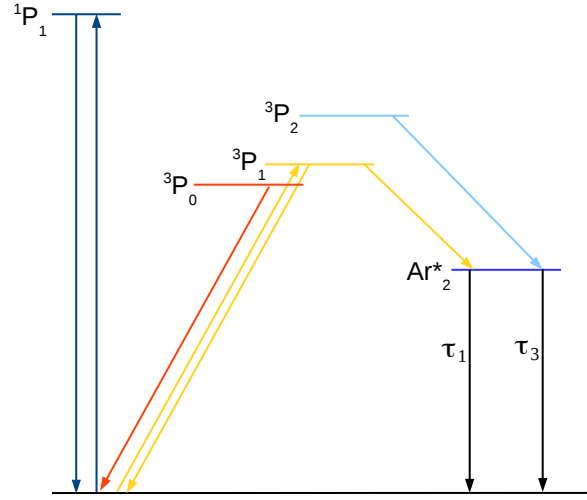
Figure 3.2: Diagram of the energy level of the first few argon atomic states with the potential increasing with height (image based on [37] and [45]). The emitted photon from the excimer decay has a lower energy than any atomic absorption line, ensuring that it will not be reabsorbed in the medium.

decay to one of the allowed excited states before forming an excimer and producing a scintillation photon:

$$Ar^+ + Ar \rightarrow Ar_2^+$$
$$Ar_2^+ + e^- \rightarrow Ar^{**} + Ar$$
$$Ar^{**} \rightarrow Ar^* + \text{heat} \tag{3.2}$$
$$Ar^* + Ar \rightarrow Ar_2^*$$
$$Ar_2^* \rightarrow 2Ar + h\nu.$$
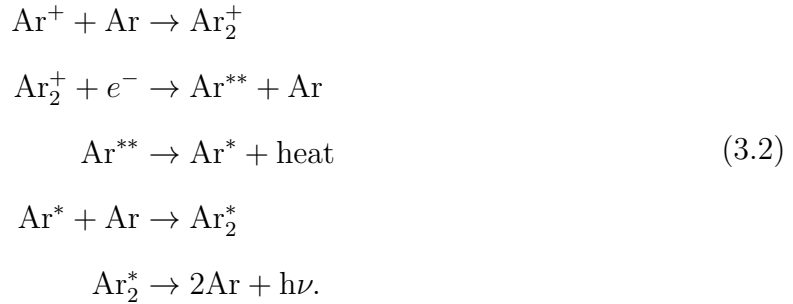
Both ionization and direct excitation of argon can cause the formation of triplet $(^3\Sigma_u)$ and singlet $(^1\Sigma_u)$ state excimers. The $^1\Sigma_u$ state follows an allowed transition of $^1\Sigma_u$ $Ar_2^* \rightarrow$ $2Ar + h\nu$ and does so in a characteristic time, τ_1. The $^3\Sigma_u$ state decay is dipole-forbidden and therefore has a longer characteristic decay time τ_3, the values of which are given in Table. 3.2. This difference in the state decay time gives the characteristic slow and fast light observed after a particle interaction in argon [24]. Both argon and neon share this large time separation, which makes them excellent candidates for single stage scintillation

Table 3.2: Characteristic decay lifetimes of the singlet and triplet states in the common noble liquids [30].

	Singlet τ_1 (ns)	Triplet τ_3 (ns)
Neon	18.2 ± 0.2	14900 ± 300
Argon	7.0 ± 1.0	1600 ± 100
Xenon	4.3 ± 0.6	22.0 ± 2.0

Table 3.3: Intensity proportion of singlet to triplet states produced in liquid Ar &Xe [24].

	Electrons (I_s/I_t)	αs (I_s/I_t)	Fission Products (I_s/I_t)
Argon	0.3	1.3	3.0
Xenon	0.05	0.45 ± 0.07	1.6 ± 0.2

detectors based on pulse shape discrimination (Section 3.1.2). The characteristic lifetimes of the two states for different noble liquids are summarized in Table. 3.2.

3.1.2 Pulse-shape Discrimination

Any scintillation producing interaction will produce both triplet ($^3\Sigma_u$) and singlet ($^1\Sigma_u$) state excimers, the proportions of which are set by the linear energy transfer, dE/dx, (LET) of the incident particle or radiation. A higher LET deposits more energy over a given distance producing more $^1\Sigma_u$ states [19]. Electronic events are not as easily absorbed as nucleons, causing a much lower LET for electronic events and therefore a great disparity in the $^1\Sigma_u$ to $^3\Sigma_u$ states produced. Using these properties it is possible to separate events into electronic events (γ or β) from nucleon events (neutron, α, or WIMP) by looking at the timing distribution in the events' scintillation light; the proportion of states is shown in Table. 3.3. By looking at the timing of the scintillation from an event, important information about the event type can be deduced. This process known as pulse-shape discrimination (PSD) has been shown by the DEAP/CLEAN collaboration to be an accurate metric for distinguishing between nuclear recoils and electromagnetic events [9].

As a proxy for measuring the LET of an event, the fraction of prompt light is used as it is sensitive to changes in the LET of an event while being simple to measure. This quantity is known as Fprompt. The larger proportion of longer lived $^3\Sigma_u$ states in γ or β events means a lower Fprompt than that of a nuclear recoil event. The significant difference in

the decay time between states in argon (see Table. 3.2) allows for the determination of the incident particle type from the events prompt charge and Fprompt alone [9].

Fprompt is calculated by integrating the resulting charge about the primary peak in a short time window (τ_{short}) and dividing that by the charge in a much longer time interval (τ_{long}):

$$\frac{\int_0^{\tau_{short}} f(t)dt}{\int_0^{\tau_{long}} f(t)dt} \tag{3.3}$$

The current DEAP-3600 short and long window durations are 140 ns and 6000 ns respectively.

A plot of calibration events depicting the Fprompt event separation from the DEAP-1 prototype is shown in Fig. 3.3. This method of PSD using Fprompt is the same as to be used in DEAP-3600. The accurate separation between electronic and nuclear recoil events is crucial in argon based detectors due to the natural occurrence of ^{39}Ar in atmospheric argon which causes a β-decay background at a 1 Hz/kg rate. DEAP-3600 has two levels of PSD, a course background reduction level and a more precise version done in data analysis once the event has been saved to disk. The introduction of the PSD based trigger to mitigate these events is extensively covered in Chapter 4.

3.2   DEAP Detectors

The DEAP experiment uses a single phase PSD detection scheme whereby scintillation is the only signal detected as previously discussed. The predecessor to DEAP-3600 was the DEAP-1 prototype detector which established the construction techniques and background mitigation used in DEAP-3600 [37]. The DEAP-1 detector, shown schematically in Fig. 3.4, has been operating since 2006.

DEAP-3600, the second DEAP collaboration detector now nearing completion, succeeds the DEAP-1 proof of concept design. The primary sections of the detector from early construction are shown in Fig. 3.5; Fig. 3.6 shows a rendering of the detector with its main components labelled.
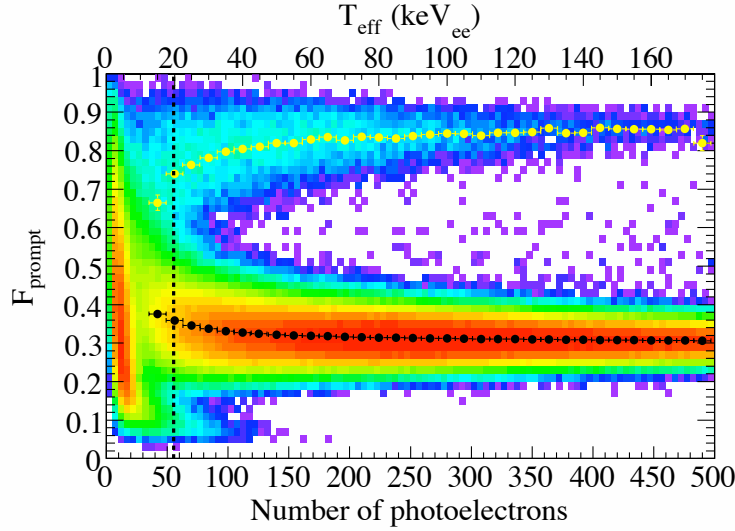
Figure 3.3: DEAP-1 Fprompt and energy distribution of neutron and γ argon scintillation events from an Am-Be calibration source. Nuclear recoils from incident neutron are in the upper band (yellow), the lower band (black) is that of γ-ray interactions. It is this separation between event types that allows for background suppression of β & γ events in DEAP-3600.

The detector is located 2 km underground in Sudbury, Ontario at SNOLAB which provides 6010 meters of water equivalent (m.w.e) shielding, reducing the cosmogenic muon flux. The 2-inch thick ultra-clean inner acrylic vessel (AV) is 170 cm in diameter and holds 3.6 tonnes of liquid argon. Events that occur near the surface are removed leaving a final fiducial volume of 1000 kgs in the central detection zone. The AV is coated with the wavelength shifter TPB, which is required for the PMT detection. Light guides are attached to the AV which serve to insulate the PMTs from the target mass allowing a higher operating temperature. The light guides also serve as neutron absorbers along with the high density polyethylene filler material. A total of 255 inward-facing, eight-inch Hamamatsu R5912 high quantum efficiency photo multiplier tubes (PMTs) are used for detection and are each attached to a PMMA (polymethylmethacrylate) light guide. A stainless steel shell surrounds the AV acting as both support and as to seal the container. The detector is housed in a 8-meter diameter water tank to provided additional shielding. There are 48 Hamamatsu 1408 PMTs attached to the detectors exterior that are used to veto any Cherenkov light caused by incident muons (primarily from decays within the
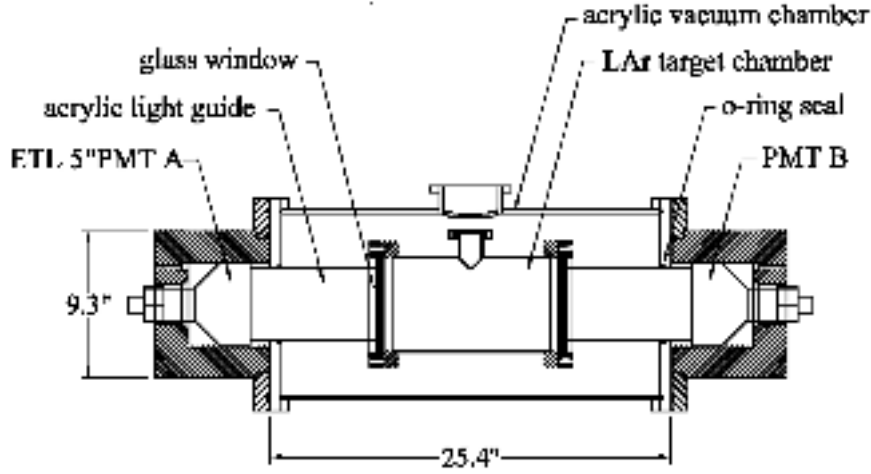
Figure 3.4: Schematic design of the DEAP-1 detector configuration. Liquid argon is held within the central stainless steel chamber. The chamber is lined with an inner acrylic cylinder and a diffuse reflector. TPB is coated on the inner detector surface to wavelength-shift the scintillation light from 128 nm → 425 nm. The shifted light is transmitted to the PMTs through PMMA (polymethyl methacrylate) acrylic light guides, thermally insulating the PMTs and shielding the argon from any neutron sources in the PMTs. The latest version of DEAP-1 is outfitted with the same PMTs as used with DEAP-3600. Image from: [10].

mine) [37]. The veto system and the water tank act as both a passive shield and as an active rejection system for any surviving cosmogenic or subterranian muons. Construction of DEAP-3600 is complete. Cool-down and argon-filling is currently underway.

The hyper-sensitivity of DEAP-3600 depends upon the low background possible, which is predicted to be about 0.6 events from all sources in the WIMP region of interest over 3 tonne-years. The detector's location at SNOLAB, with a 6010 m.w.e overburden, is well shielded from cosmogenic muons and the water tank and active muon veto system aids in further muon rejection. Materials were chosen to be low in neutron or alpha sources, all materials being prepared in low-radon environments. An in-depth discussion on the preparation of low background components is covered in Ref. [18]. The total expected event rates for DEAP-3600 are given in Table 3.4.

The dominant background will be that of naturally occuring ^{39}Ar β-decay at a rate of

Figure 3.5: **Left:** The acrylic vessel with light guides attached. **Center:** Detector with PMTs & foam/filler blocks installed. **Right:** Detector with steel shell and outward facing veto PMTs installed.

Table 3.4: Expected event rates in the DEAP-3600 detector at SNOLAB [8].

Event	Rate (Hz)
^{39}Ar β-decay	3.6×10^3
Surface Background	$< 10^{-3}$
Cosmic Muons	$< 10^{-3}$
WIMPs	$< 10^{-5}$
^{222}Rn decay	$< 5 \times 10^{-6}$
Neutron Sources in Ar	$< 10^{-6}$

~1 Hz/kg of atmospheric argon. The β-decay events cause electronic recoils in the argon and can be separated from any nuclear recoil events using PSD. Due to the high proportion of β events to expected WIMP events (a difference of 10^8), it is important to suppress β events at the trigger level. PSD reduction of β events by the trigger will minimize dead time as the digitizers will not record for all of these events. Trigger level background mitigation will also decrease the bandwidth and storage requirements of the data acquisition system (DAQ). The trigger algorithm is discussed in depth in the next chapter.
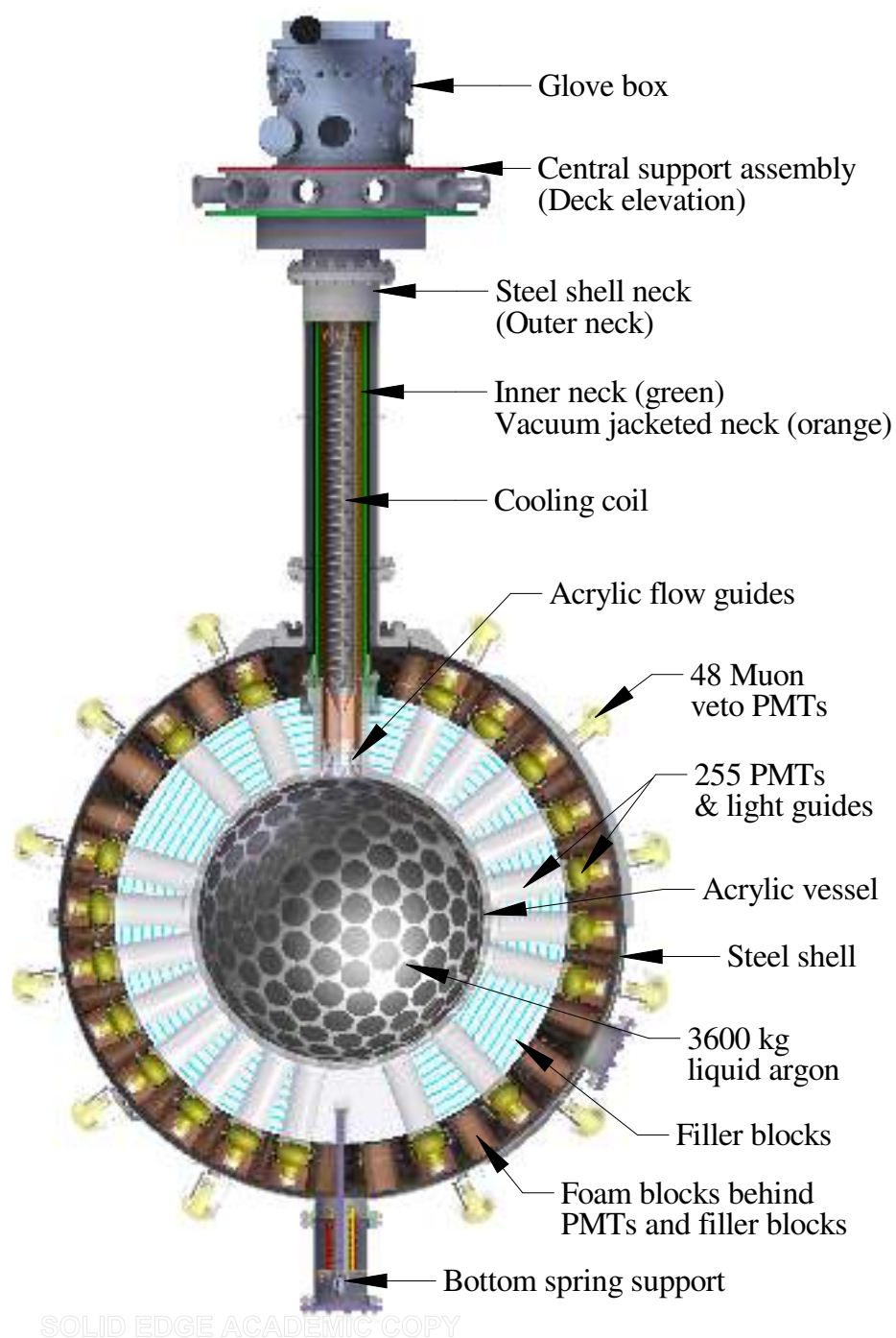
Figure 3.6: Engineering design rendering of the DEAP-3600 detector. Each of the primary components are labeled.

Chapter 4

DEAP-3600 Trigger Design & Development

The trigger design serves as an integral part of the DEAP-3600 electronics system. The trigger logic is implemented on an Altera Stratix IV field programmable gate array (FPGA) which is located on the rack mounted digital trigger module (DTM) which controls the DEAP-3600 data acquisition system (DAQ). This chapter discusses the electronics system as well as the trigger design and implementation.

4.1 Electronics

The electronic architecture is divided into 3 different systems: the front end, trigger, and data acquisition as shown in Fig. 4.1.

4.1.1 Front End

The front end receives a signal from each of the PMTs through the signal conditioning boards (SCBs). The 22 primary and four veto SCBs provide several functionalities including high voltage decoupling and protection, cable termination, pulser inputs for artificial pulse injection (PPG), an analog sum of the PMT inputs, and a high and low gain output for each channel. The SCBs minimize the signal to noise seen by the digitizers by reshaping
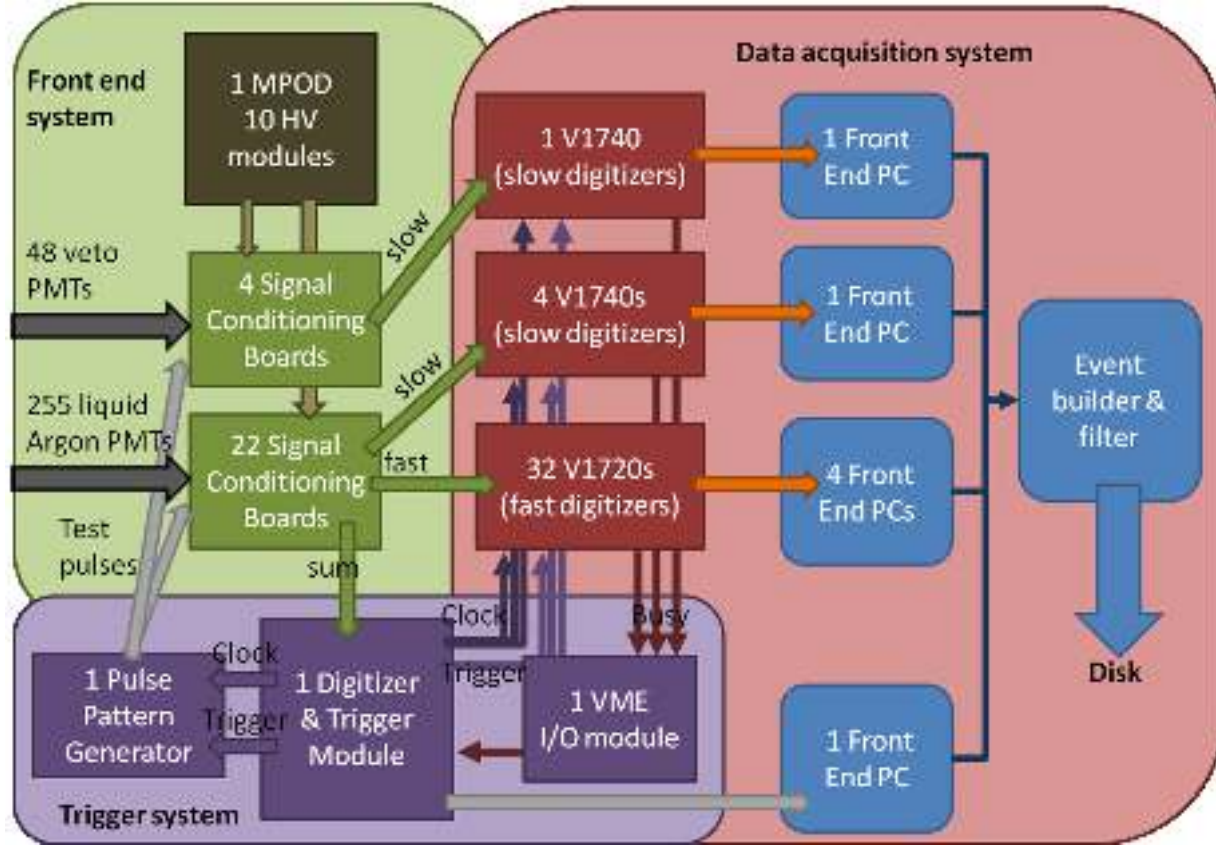
Figure 4.1: Diagram of the architecture design and data flow in the DEAP-3600 electronics system. Image credit: DEAP Collaboration.

the signal pulses. The high gain output goes to the CAEN V1720 digitizers and its pulse width is slightly widened to allow pulses to be properly handled by the digitizer. The low gain output's pulse width is widened more than the high input and is passed to the slower CAEN V1740 digitizers. The SCB also outputs a single analog sum of its 12 PMT inputs which is passed to the triggers digitizer board.

4.1.2 Trigger

The trigger system consists of a digital trigger module (DTM), shown in Fig. 4.2 and schematically in Fig. 4.3, and a pattern pulse generator (PPG). The primary motherboard of the DTM has three Xilinx Spartan-6 LX FPGAs which interface with three detachable daughter mezzanine boards. The mezzanine boards used in the newest DTM arrangement are a 24-channel ADC board with three eight channel 12-bit 50 MHz ADCs; a 12-channel

I/O board; and a 62.5 MHz clock board. The current DTM configuration used outputs a master clock from this mezzanine that is daisy chained to the rest of the system. A new version, currently in the end stages of development, replaces the DTM sourced master clock with an external master clock board as is discussed in Section 4.4. The motherboard is equipped with an Altera Stratix IV GX FPGA which is used as the primary processing and communication driver for the DTM. It is this primary FPGA that the triggering firmware is implemented on.

The DTM receives 22 analog sums (ASUMs) of 12 PMT signals from the SCBs which are digitized by the ADC mezzanine board. The DTM is constantly integrating the ASUMs and uses Fprompt and charge to make a triggering decision. If the triggering requirements are met (as discussed in Section 4.2) the DTM will send a trigger command through the I/O board sending a signal to the first in a chain of digitizers which passes the trigger along to the rest in a daisy-chain arrangement.

The other main component in the trigger is the pattern pulse generator (PPG). This board generates test signals to the SCB for self-test. Inspection of these pulses serve as a stress-test for the system and is used to test for data irregularities.

4.1.3 Data Aquisition

The data acquisition system digitizes and saves to disk the signals from each PMT passed from the front end SCBs. The high gain SCB signals are passed to an array of 32 CAEN V1720s, which are eight-channel, 12-bit waveform digitizer modules that sample at 250 MS/s. The low gain signals are passed to four CAEN V1740s which are 64-channel 12-bit waveform digitizer modules that sample at 62.5 MS/s. The slower V1740s are used with lower gain to record any events that saturate the range of the V1720s. The current state of the digitizers and their control is handled by logic on the Stratix IV FPGA.

Figure 4.2: The digital trigger module populated with the ADC, trigger I/O, and the clock mezzanine boards. Digital control is implemented on an Altera Stratix IV GX field programmable gate array.

4.2   Trigger Algorithm

The Fprompt trigger analyses the 22 SCB ASUM signals through the ADC mezzanine board. The signals are constantly digitized and are digitally summed together into an ASUMSUM. The firmware performs a rolling integral over a short and a long time window nominally 140 ns and 6.0 μs. The Fprompt is not explicitly calculated however it is used for event selection; for a defined Fprompt an event is recorded if

$$E_{long} > E_{thres} \ \& \ E_{long} > [E_{short} \times F_{thres}]. \tag{4.1}$$

Events are sorted using the short energy and Fprompt into one of six regions as depicted in Fig. 4.4.

The beginning of the event is taken as the first bin in the short window that maximizes
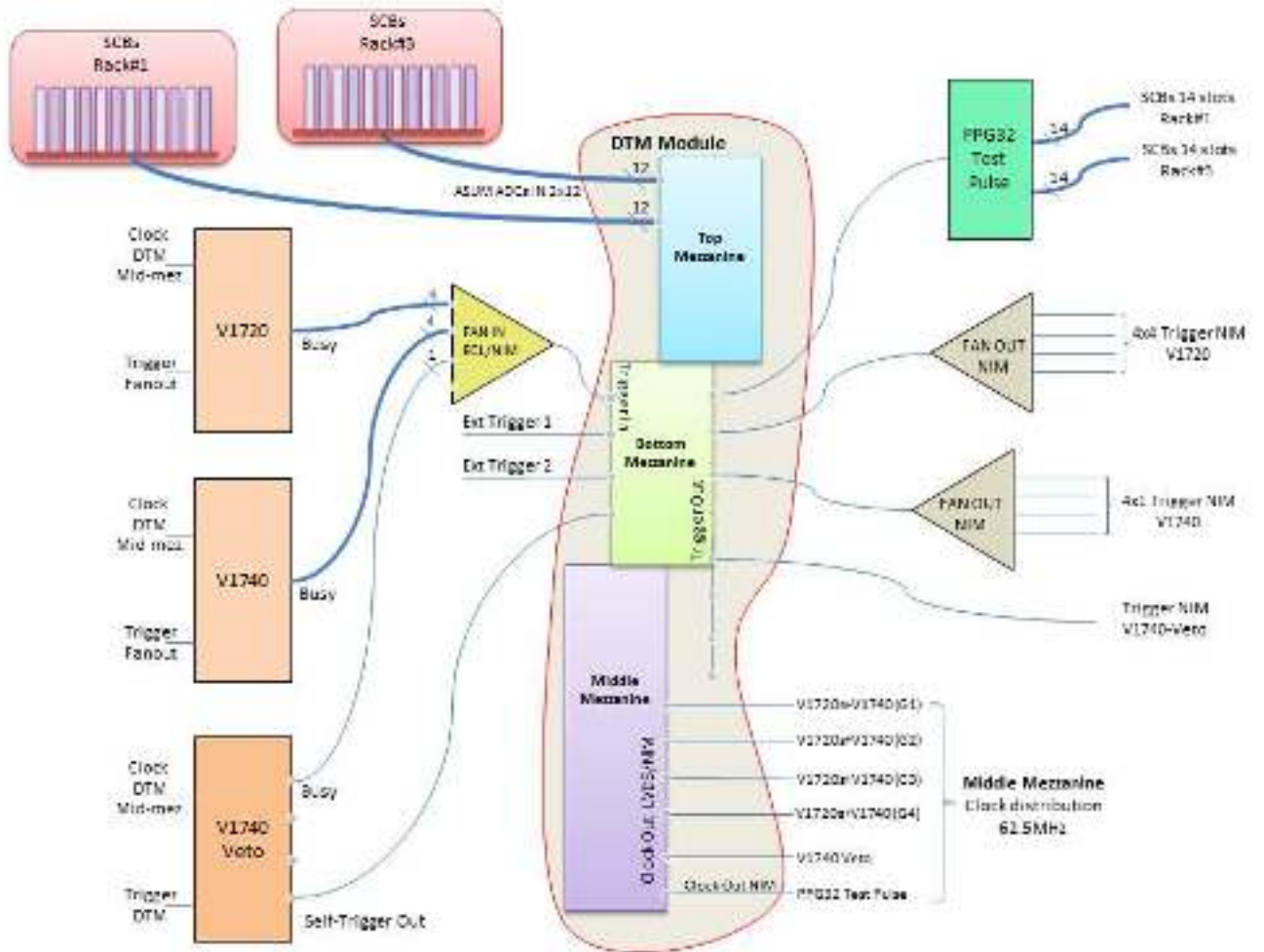
Figure 4.3: Diagram of the information and signal flow in the DTM.

the charge in that window. If the next bin in the rolling integral is lower then the last, the trigger continues to integrate forwards for a defined look ahead time (nominally 5 bins (80 ns)) to avoid local minima. If the total integrated charge does not increase past the maximum total charge within the look ahead time, then the first event bin is set as that of the maximum charge window. As the long window is integrated, a triggering signal will occur immediately a trigger condition has been meet even if the integration of the long window has not yet finished. Therefore, as multiple trigger regions (see Fig. 4.4) can be passed for a single event, the final trigger type coincides with the maximum Fprompt and short window charge reached.
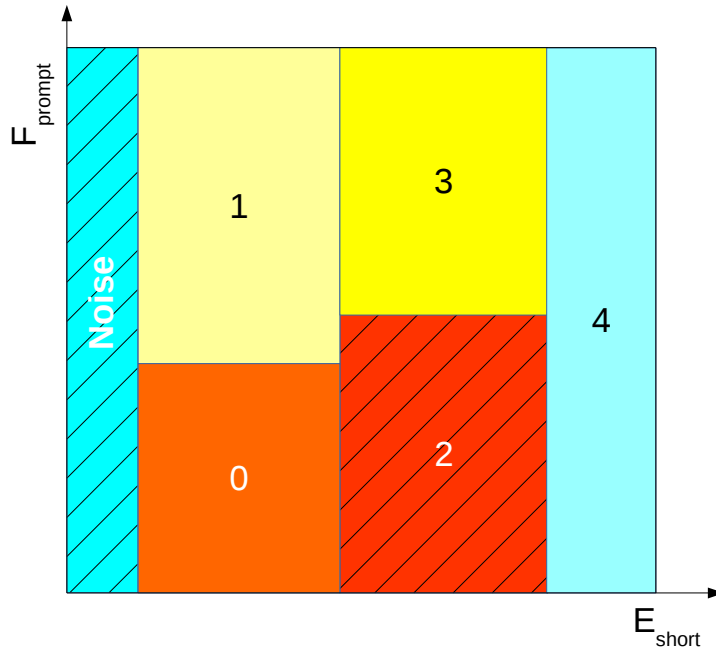
Figure 4.4: Trigger regions as used in the pulse shape discrimination background rejection method. Noise in the PMTs fall under very low energy and β events are grouped into high energy low Fprompt. The WIMP region of interest is at high Fprompt and could fall into either region of energy.

Although the noise rate in the WIMP region of interest (centre one tonne fudicial volume, energy $<$ 100 keV [18]) is anticipated to be very low, ^{39}Ar β-decay occurs at a high rate as shown in Table 3.4. The Fprompt trigger uses pulse shape discrimination to mitigate (or pre-scale) β events, reducing their recorded rate on the order of 50 times. If an event is pre-scaled the time and charge of the event is recorded, but no digitizers are triggered. To maximize sensitivity the trigger should have a low possibility of discarding events while busy, ensuring that if an event of interest occurs (WIMP or non β background event), it will be recorded. For highest sensitivity, pre-scaling should be done only on PMT dark noise events and β events, so the probability of miscategorization and subsequent pre-scaling of rare events must be well understood and minimized.

In addition to the Fprompt trigger, there is a periodic trigger, an exponential random trigger which triggers the system following an exponential random variable probability distribution, and an external trigger input from the PPG. These triggers are primarily used for diagnostic tests and calibration.

4.3　Trigger Firmware Implementation

The work done on the trigger firmware follows work done by several other DEAP collaborators, notably Yair Linn and Sebastian Dittmeier at TRIUMF. This project started with an untested trigger and development here began at the debugging and testing phase.

Altera Quartus 13.0sp1 integrated development environment and the ModelSim logic simulator were used for compiling and simulation. Each change to the logic was thoroughly simulated with real waveforms from DEAP-3600 to ensure no functional regressions due to the logic. Following simulation testing, the logic is loaded onto the same hardware used in the detector. Using an arbitrary waveform generator, the trigger's functionality is confirmed. At this point the new logic release is loaded remotely onto a second DTM at SNOLAB. This DTM then replaces the currently installed DTM to ensure that were a bug to slip by, detector time is not lost as the previous firmware can be reverted to by simply replacing the DTM boards.

Once an operational firmware release has been installed in the detector a series of tests is run on each of the DTM functions. Using LED light injection into the detector (see Section 5.1) triggered events are recorded along with the waveforms from the ASUMSUMs. The DTM trigger decision is then reproduced through a C++ ROOT macro [11] using the waveform readout (developed by Ben Smith at TRIUMF). If irregularities in the triggering decision are found, the waveform is then put through a ModelSim simulation of the trigger logic to see if the decision is reproducible or if an error has occurred.

Following this development stream, functioning Fprompt trigger logic has been installed in the DEAP-3600 detector. Chapter 5 discusses the study and characterization of the Fprompt trigger's behaviour and efficiency in the turn on region.

4.4　Hardware Updates

Currently the clock distribution and thereby the synchronization of events for the DTM and the V1720 and V1740 digitizers is done through a daisy chain arrangement. The master clock is generated on the DTM at 50 MHz, a phase lock loop (PLL) raises the frequency to

100 MHz for the periodic trigger, and 62.5 MHz clock for the trigger clocking and digitizer clocks. The dedicated clock fan out mezzanine board passes the 62.5 MHz clock to the first digitizer in groups of at most six which is then passed along the chain. Each digitizer has a calculated clock phase offset to address latency in the chain as described by the manufacturer [13].

The stability of this arrangement has been brought into question and therefore a new clock distribution system has been developed. The clock fan out mezzanine on the DTM is to be replaced with a mezzanine board that receives a clock from a dedicated external master clock generator. This clock generator distributes a 62.5 MHz clock to each of the digitizers and DTM over identical connections removing the need for an introduced clock offset. This clock arrangement should prove to be more stable, ensuring the correct synchronization of events in the DAQ.

Additionally the mezzanine board that replaces the dedicated master clock fan out board on the DTM has added functionality which allows for the direct readout of internal FPGA registers over a gigabit ethernet connection. The introduction of this system will both increase clock stability and allow for more diagnostic tests from the ethernet readout. The development of this system has recently been completed but has yet to be tested.

The study discussed in Chapter 5 uses the daisy chain clock distribution scheme and development of the new system is still on going.

Chapter 5

Trigger Analysis & Characterization

The following chapter discusses the experimental testing and characterization of the trigger once installed in the detector. To maximize the sensitivity of the detector, it is crucial that the behaviour of the trigger be well understood. Using a system of light injection, the statistical efficiency of the DTM is analysed. The DTM's efficiency at the trigger threshold crossing will be used to set the event sorting thresholds for energy regions as discussed in Section 4.2.

5.1   AARF Light Injection

The acrylic reflector and fibre optics (AARF) system serves as a permanent light injection system for the DEAP-3600 detector. The AARFs are designed to calibrate the charge generated by a single photon at the beginning of a data run. Additionally the AARFs are used for calibration of PMT timing and detector stability with time [12].

The AARF system uses aluminium coated acrylic reflectors to inject 435 nm LED light, over an acrylic fibre onto a host PMT, as shown in Fig. 5.1. DEAP-3600 is outfitted with 20 PMT AARFs with an additional two reflectors in the neck of the detector with no host PMT. In a PMT AARF 97% of the injected light in found in the host PMT, with only 3% reflected onto its surrounding neighbours [12]. The neck AARFs, without a host PMT, allows for more evenly distribution of light over the detector.
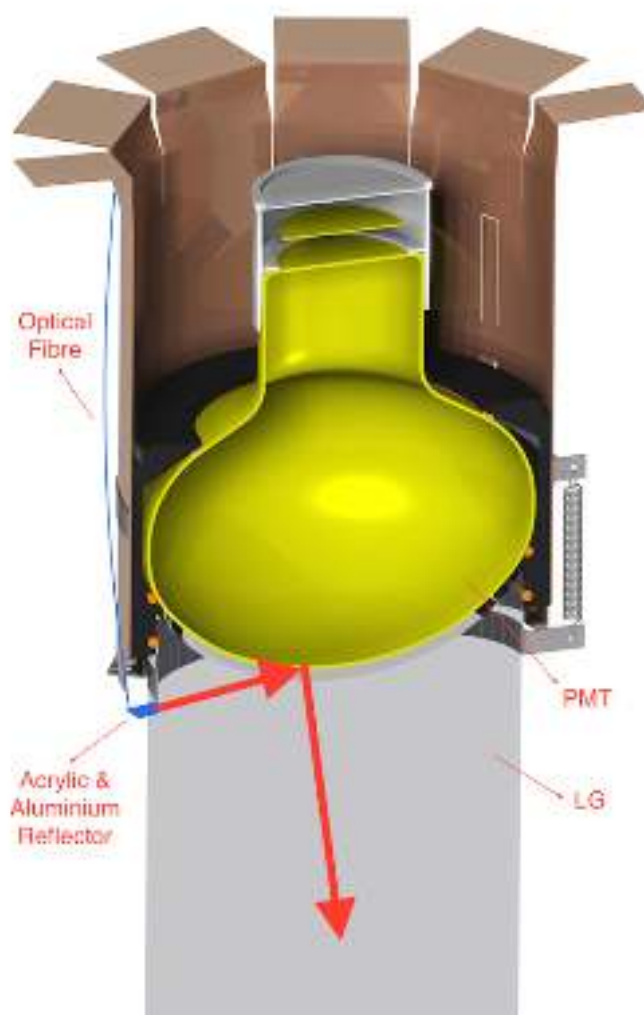
Figure 5.1: Rendering of the light injection system for a PMT AARF. Light from a 435 nm LED is passed over an acrylic optical fibre and reflected off an aluminium coated acrylic reflector onto the host PMT.

5.2   Efficiency Study

Light injection using the AARF system was used for finding the efficiency of the DTM. The triggering algorithm is as follows:

1. A DTM periodic trigger is sent to the AARFs

2. The AARFs send an external pulse to the DTM causing the V1720 digitizers to begin recording

3. The AARF LED pulses, injecting light into the detector

4. The DTM integrates the charge from the PMTs, if the set threshold for total short energy is meet, a DTM event will be recorded.

5. Every AARF event's integrated V1720 charge is recorded in a histogram, if a DTM event occurs a second histogram is filled with the event indicating the events that passed the threshold.

Using this trigger scheme, the outputs and settings of which are given in Table 5.1, the efficiency at a threshold crossing can be analysed.

Table 5.1: Triggers and output setting used for periodic light injection efficiency study corresponding to run types 304-306 (see Table 5.2).

Trigger	Rate (Hz)	Outputs	Prescaler
Periodic 0	1500	V1720, Calib, AARF	1
Periodic 0	1500	V1720,V1740, Calib, AARF	5
Periodic 1	56	V1720	1
ADC High Energy	N/A		1
ADC High Energy	N/A	DTM	100

In this study Fprompt is not taken into account and therefore a trigger will be generated by the DTM for any event that has the set threshold charge integrated over a set number of clocks (denoted as short window in Table 5.2).

5.2.1 Data Taking

Data runs were taken at three different DTM thresholds where it is estimate the low, medium, and high energy cuts will be made for the trigger level PSD. The runs were then preformed for several different intensities of the AARFs, ensuring good statistics across the threshold crossing region. The AARF light is very prompt, as is to be expected; Fig. 5.2 - 5.4 show typical ASUMSUM DTM waveforms for three AARF intensities and the associated charge-Fprompt relation. The charge is given in photo electrons (PE) measured by the V1720s utilizing photon counting to reduce uncertainty. The data run summaries are given in Table 5.2.

Table 5.2: Data run descriptions for trigger efficiency study. Run numbers sharing a run type denote a change in AARF intensity only.

Run	Type	AARF Intensity	DTM Threshold (ADC)	Short Window (ns)
15826	304	1270	1400	128
15827	304	1300	1400	128
15828	305	1530	6000	128
15829	305	1560	6000	128
15830	306	1835	15000	128
15831	306	1870	15000	128

The data runs for a single DTM threshold are combined into a single histogram to ensure a range of charge near the DTM threshold. These histograms are plotted in superimposed pairs in Fig. 5.5 - 5.7.

Figure 5.2: **Left:** Typical AARF DTM waveform for an intensity of 1270. **Right:** Fprompt against number of photo electrons recorded per event at an AARF intensity of 1270
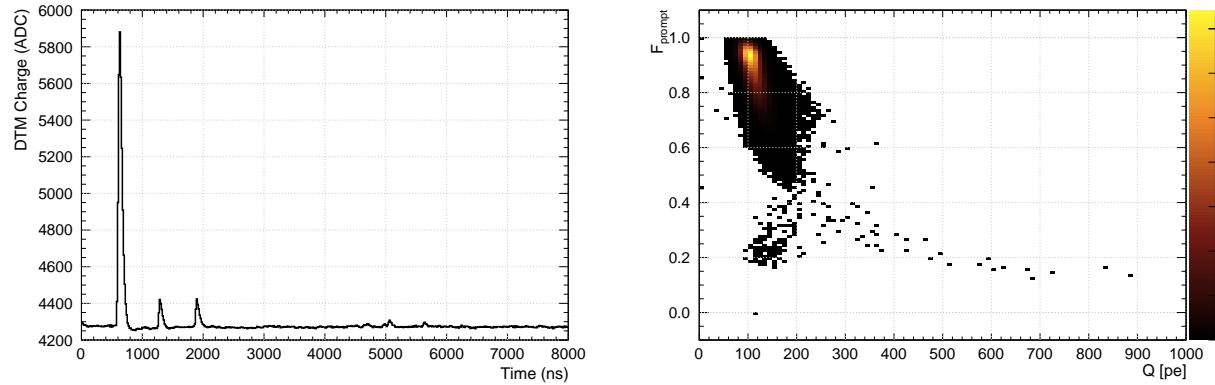
Figure 5.3: **Left:** Typical AARF DTM waveform for an intensity of 1530. **Right:** Fprompt against number of photo electrons recorded per event at an AARF intensity of 1530
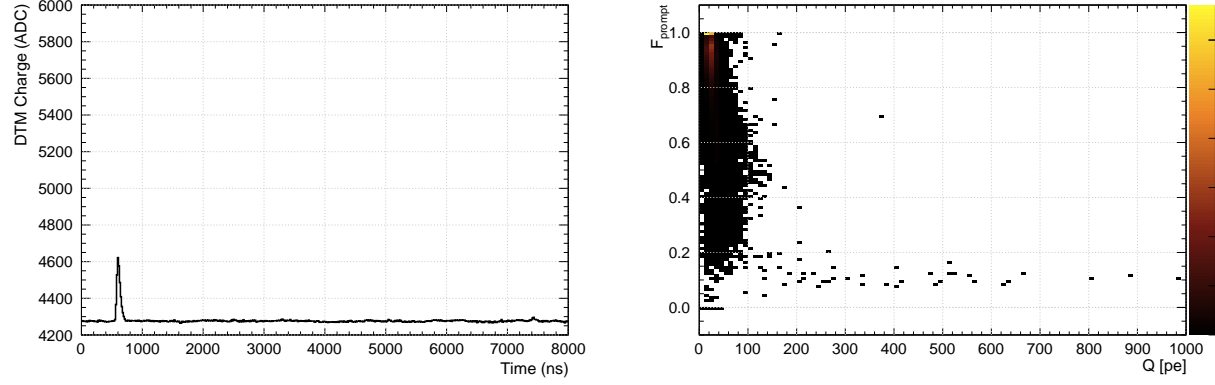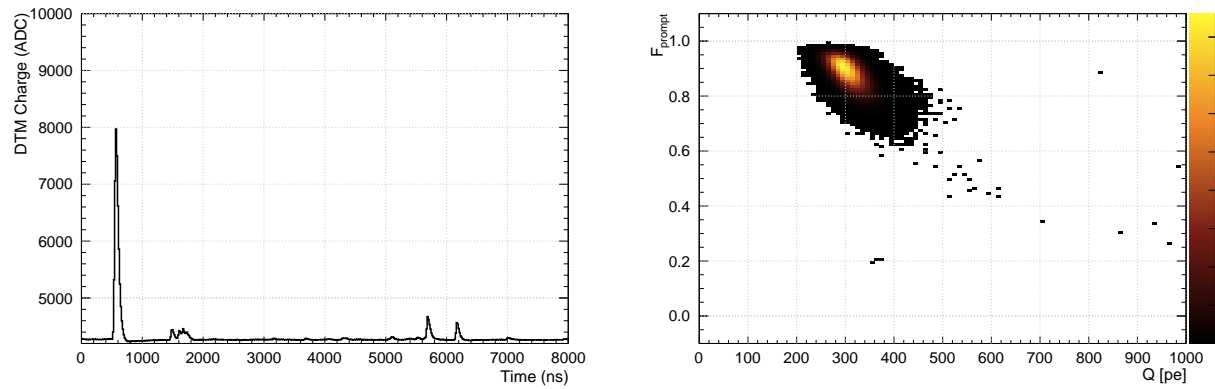
Figure 5.4: **Left:** Typical AARF DTM waveform for an intensity of 1870. **Right:** Fprompt against number of photo electrons recorded per event at an AARF intensity of 1870
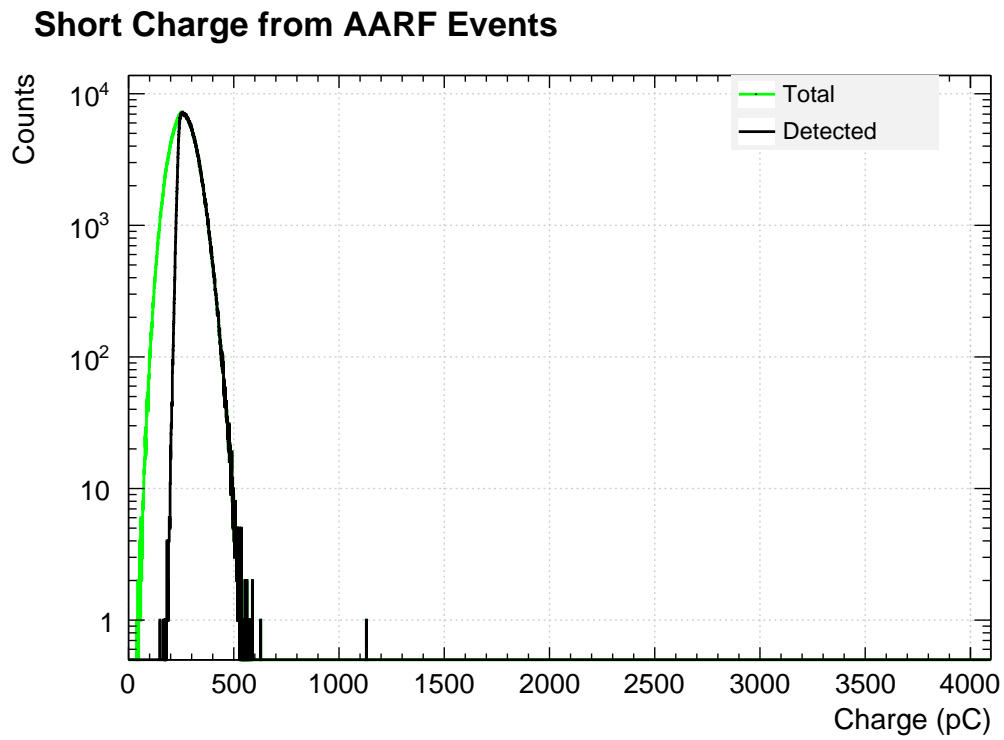
Figure 5.5: Histograms of the total light injection events (green) and the events recorded by the trigger (black) for a DTM threshold of 1400 ADC
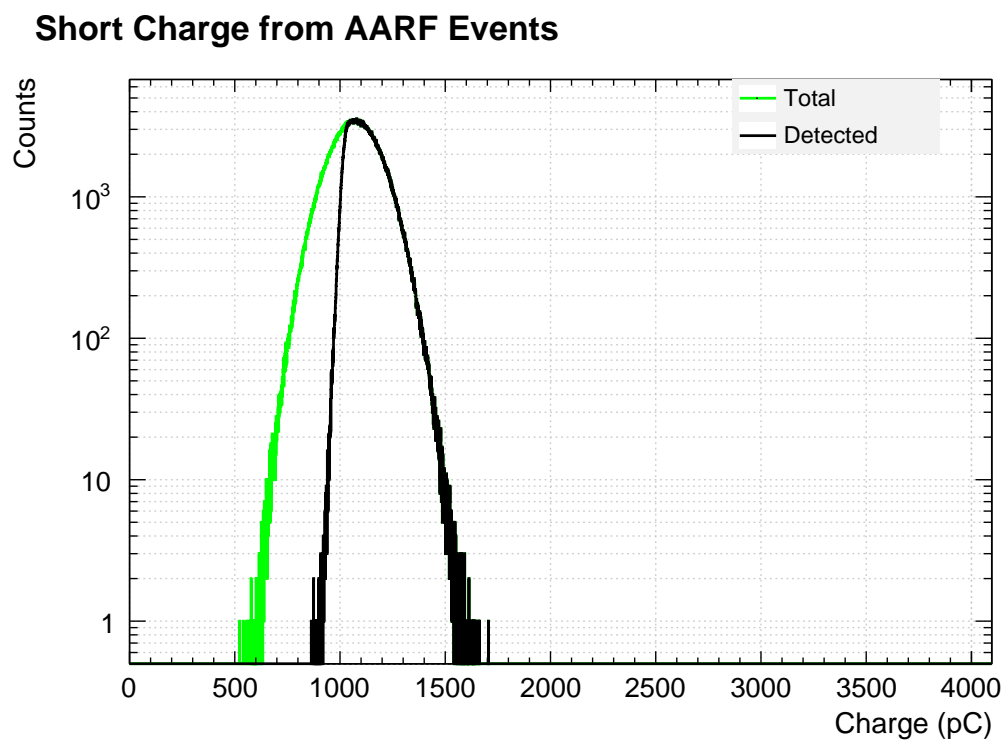
Figure 5.6: Histograms of the total light injection events (green) and the events recorded by the trigger (black) for a DTM threshold of 6000 ADC

Figure 5.7: Histograms of the total light injection events (green) and the events recorded by the trigger (black) for a DTM threshold of 15000 ADC

5.3   Error Analysis and Erf Fitting

The quantity of interest here is the efficiency that an event is recorded by the DTM given the value of the V1720 digitizers. Following the work done by Paterno (2004) [36], the uncertainty calculation for the data selection is derived from the application of Bayes's theorem.

5.3.1   Bayesian Errors

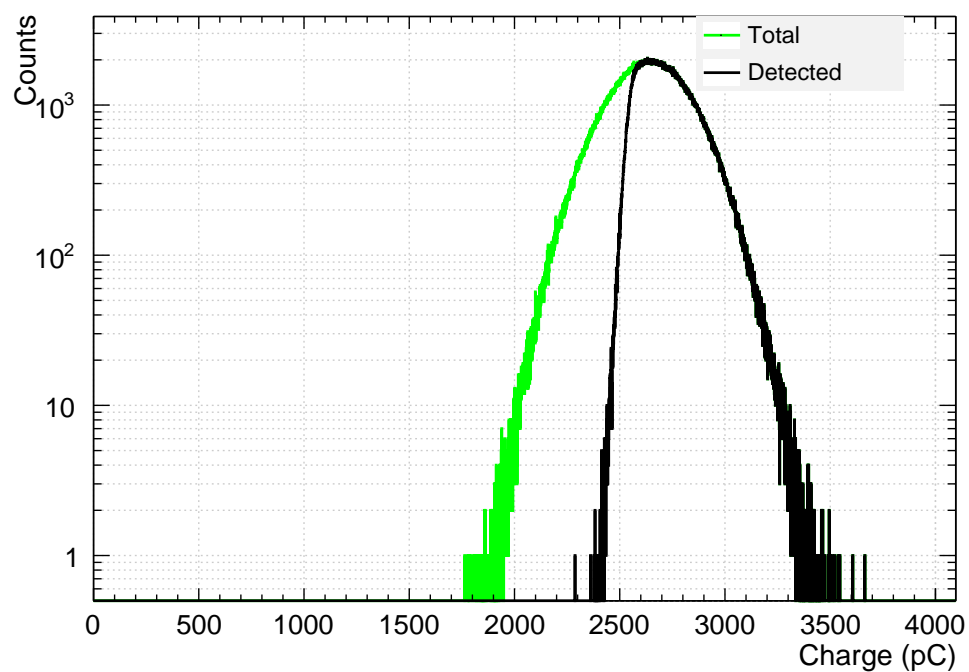For a total of N events in a sample passing a data cut, a probability of selection ϵ, and relevant prior information I, the probability that k events are selected is given by the binomial distribution:

$$P(k|\epsilon, N, I) = \frac{N!}{k!(N-k)!}\epsilon^k(1-\epsilon)^{N-k} \tag{5.1}$$

Here we are interested in finding the value of ϵ from $k, I, \& N$ which are known values. By applying Bayes's theorem to the binomial distribution, the probability that the true selection probability is between ϵ and $\epsilon + \mathrm{d}\epsilon$ $(P(\epsilon|k, N, I))$ can be determined:

$$P(\epsilon|k, N, I) = \frac{P(k|\epsilon, N, I)P(\epsilon, N, I)}{Z}. \tag{5.2}$$

Here Z is a normalization constant defined as:

$$Z = \frac{N!}{k!(N-k)!}\int_0^1 \epsilon^k(1-\epsilon)^{N-k}d\epsilon. \tag{5.3}$$

Applying the definition of the beta function:

$$B(x,y) = \int_0^1 t^{x-1}(1-t)^{y-1}dt = \frac{\Gamma(N+2)}{\Gamma(k+1)\Gamma(N-k+1)}, \tag{5.4}$$

Applying the Beta function to Eq. (5.3), a solution to Eq. (5.2) can be expressed as:

$$P(\epsilon|k, N, I) = \frac{\Gamma(N+2)}{\Gamma(k+1)\Gamma(N-k+1)}\epsilon^k(1-\epsilon)^{N-k} \tag{5.5}$$

This formulation will give a most probable value of the selection probability k/N, however finding the exact uncertainty is non-trivial.

The probability that ϵ is in the range $[\alpha, \beta]$ is denoted λ and is taken in this study to be one sigma or 68.3%. λ is given by:

$$\int_{\alpha}^{\beta} P(\epsilon|k, N, I)d\epsilon = \lambda. \tag{5.6}$$

Finding the smallest interval $[\alpha, \beta]$ will give the confidence level that ϵ falls within this range. Minimizing this interval is done through the application of Lagrange multipliers, leading to the simultaneous non-linear equations:

$$G + \rho\alpha^k(1 - \alpha)^{N-k} = 0 \tag{5.7}$$

$$G + \rho\beta^k(1 - \beta)^{N-k} = 0 \tag{5.8}$$

$$B_\beta(k + 1, N - k + 1) - B_\alpha(k + 1, N - k + 1) = \lambda G. \tag{5.9}$$

Here G is $\Gamma(k + 1)\Gamma(N - k + 1/\Gamma(N + 2))$, ρ is a Lagrange multiplier and $B_x(u, v)$ is the partial Beta function defined as:

$$B_x(u, v) = \int_0^x t^{u-1}(1 - t)^{v-1}dt. \tag{5.10}$$

This error solution, formulated by Paterno (2004) [36], has been included in the ROOT data analysis framework with the TEfficiency class [11].

5.3.2 Erf Fitting

The Gaussian error function (or erf) naturally arises as the threshold of a Gaussian selection [14], such as is expected in the DTM. The erf is defined as:

$$\text{erf}(x) = \frac{2}{\sqrt{\pi}} \int_0^x e^{-\tau^2} d\tau \tag{5.11}$$

Assuming there is no significant excess noise, interference, or non-Gaussian behaviour, it is expected that the DTM efficiency as a function of the total V1720 short window charge would be well fit to an erf. If an event has a V1720 short window charge that falls within a turn on region, there is a possibility of being categorized as either of the two energy regions being transitioned between. Characterizing these regions with an erf allows for the

inclusion of this statistical possibility of being miscategorized by the DTM, and a deeper knowledge of the uncertainty. In operation the trigger regions being pre-scaled will have to be chosen is such a way to minimize the possibility of pre-scaling a non-β event while not saturating the DAQ with events. This will be done once the rate of β-decay events in the detector is appreciable as it is being filled with argon.

The histograms of the total and detected events for each AARF intensity at a given DTM threshold are combined to ensure high statistics at the turn-on region of the DTM (see Fig. 5.5 -5.7). Using the ROOT TEfficiency class, these histograms are divided to give the efficiencies shown in Fig. 5.8 -5.10. An erf function with a mean (μ) and standard deviation (σ) is fit to the turn on curves as a function of the V1720 charge (ϵ) given by:

$$f(\epsilon, \mu, \sigma) = \left(\frac{1}{2}\right)\left(1 + \text{erf}\left(\frac{\epsilon - \mu}{\sqrt{2}\sigma}\right)\right) \tag{5.12}$$

Figure 5.8: Efficiency of the trigger for a DTM threshold of 1400 ADC. The efficiency is taken from the histograms given in Fig. 5.5 and is fit to a Gaussian error function (Eq. (5.12)).
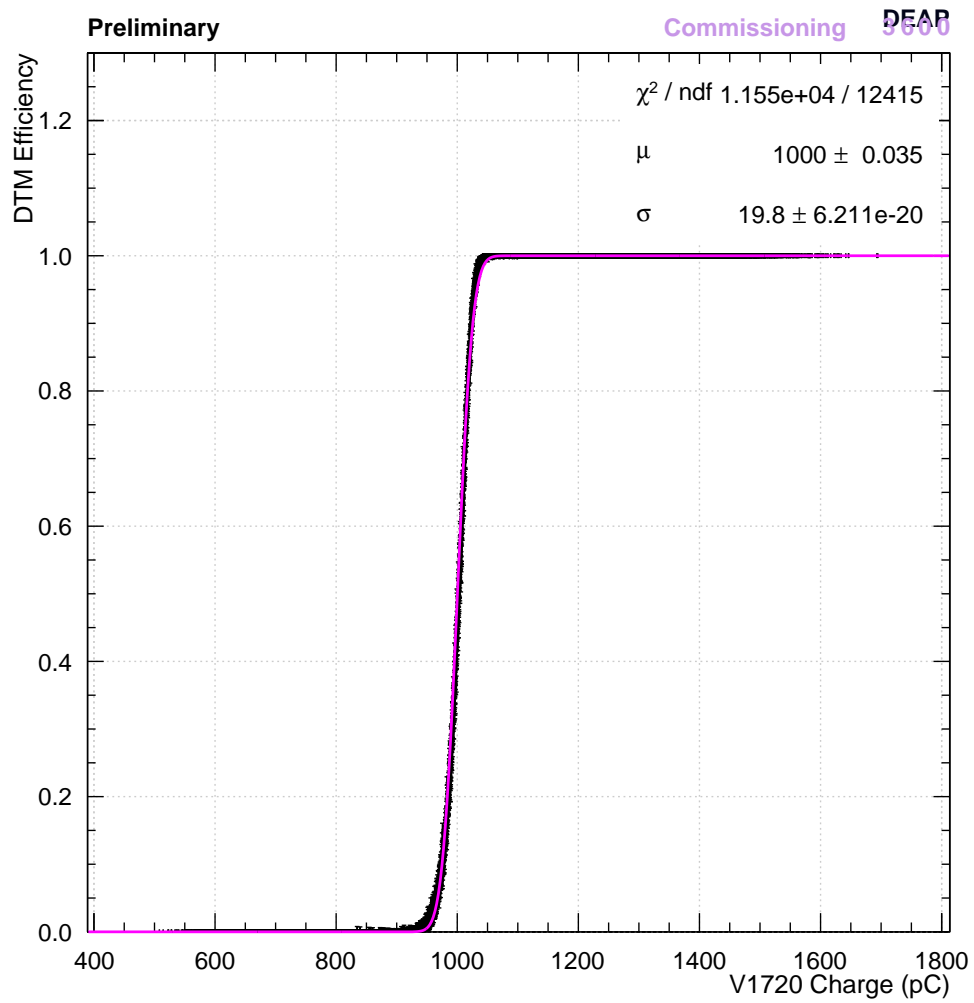
Figure 5.9: Efficiency of the trigger for a DTM threshold of 6000 ADC. The efficiency is taken from the histograms given in Fig. 5.6 and is fit to a Gaussian error function (Eq. (5.12)).

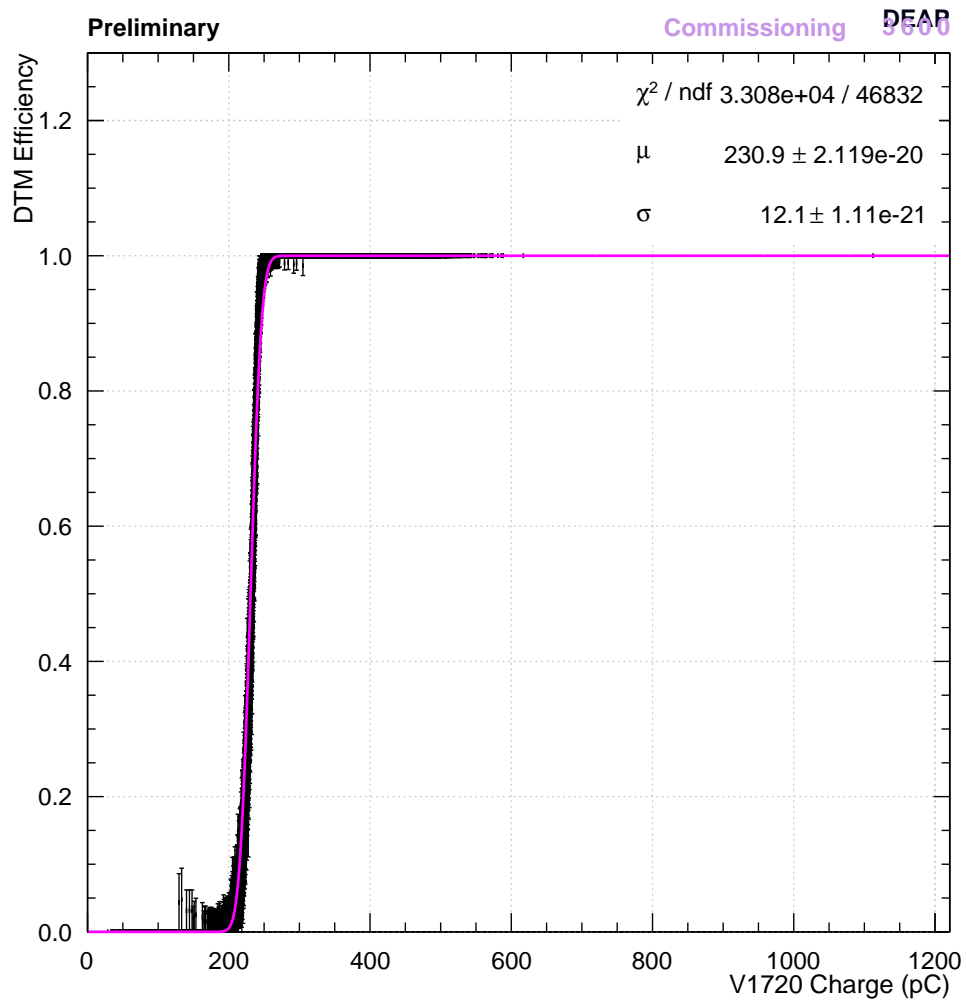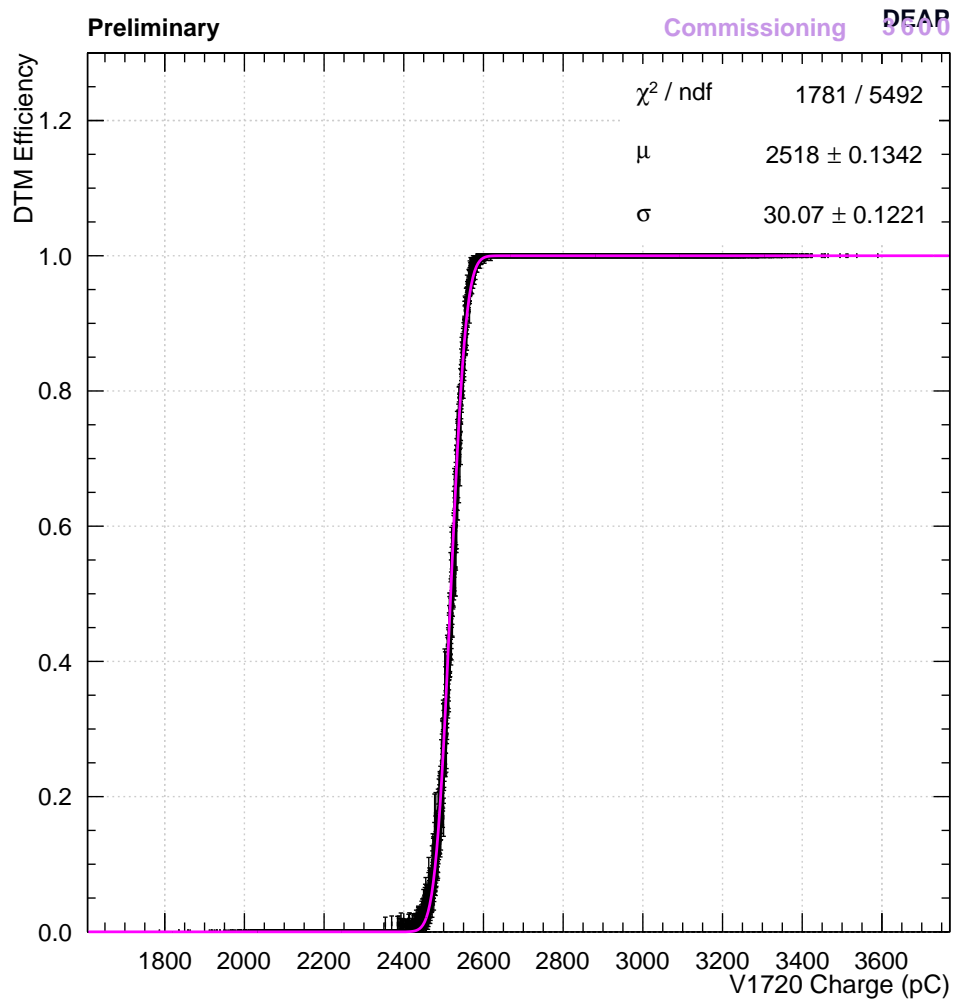Figure 5.10: Efficiency of the trigger for a DTM threshold of 15000 ADC. The efficiency is taken from the histograms given in Fig. 5.7 and is fit to a Gaussian error function (Eq. (5.12)).

The spread in the trigger efficiency is due to the differences in charge calculation between the DTM and the V1720s. The DTM receives the analog sum of the SCB inputs (the ASUMs) and integrates the digital sum of them (the ASUMSUM) over a short time window centred at an events pulse peak. The analog ASUMs receive the entire signal from the PMTs, the difference in which can be seen in the charge comparison histograms for recorded events shown in Fig. 5.11-5.13 for each of the different thresholds; note the clean cut off in the DTM charge at the DTM threshold value.

Figure 5.11: Charge histogram comparing the charge recorded by the DTM and by the V1720s for a threshold of 1400 ADC. Although quite a tight charge relation, the spread in value introduces an uncertainty causing the Gaussian shape that is seen in the efficiency analysis
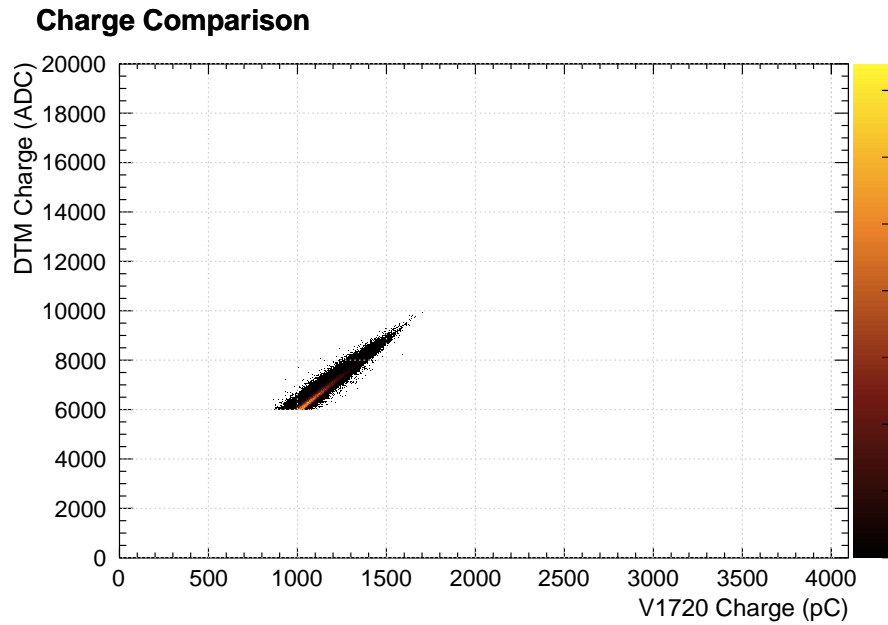
Figure 5.12: Charge histogram comparing the charge recorded by the DTM and by the V1720s for a threshold of 6000 ADC. Although quite a tight charge relation, the spread in value introduces an uncertainty causing the Gaussian shape that is seen in the efficiency analysis
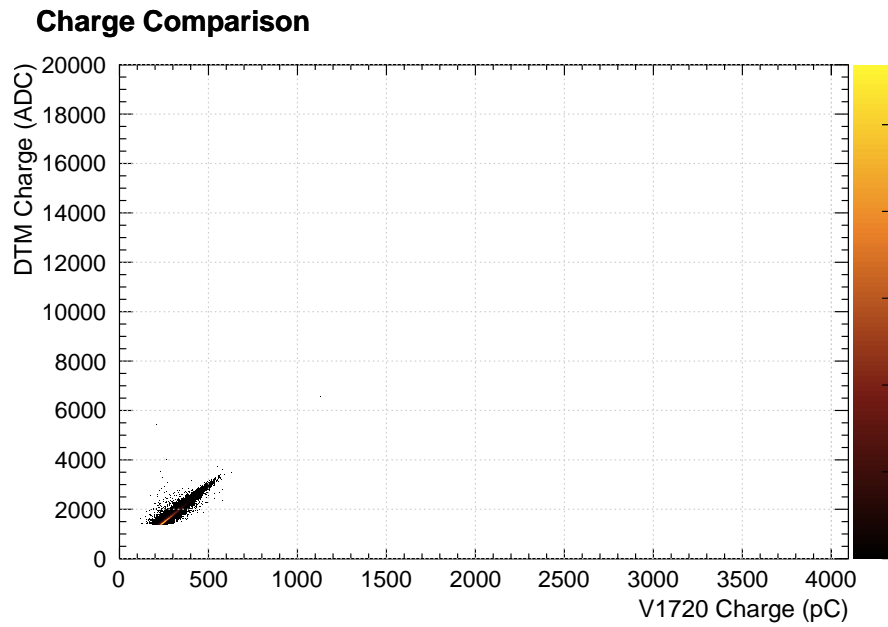
Figure 5.13: Charge histogram comparing the charge recorded by the DTM and by the V1720s for a threshold of 15000 ADC. Although quite a tight charge relation, the spread in value introduces an uncertainty causing the Gaussian shape that is seen in the efficiency analysis
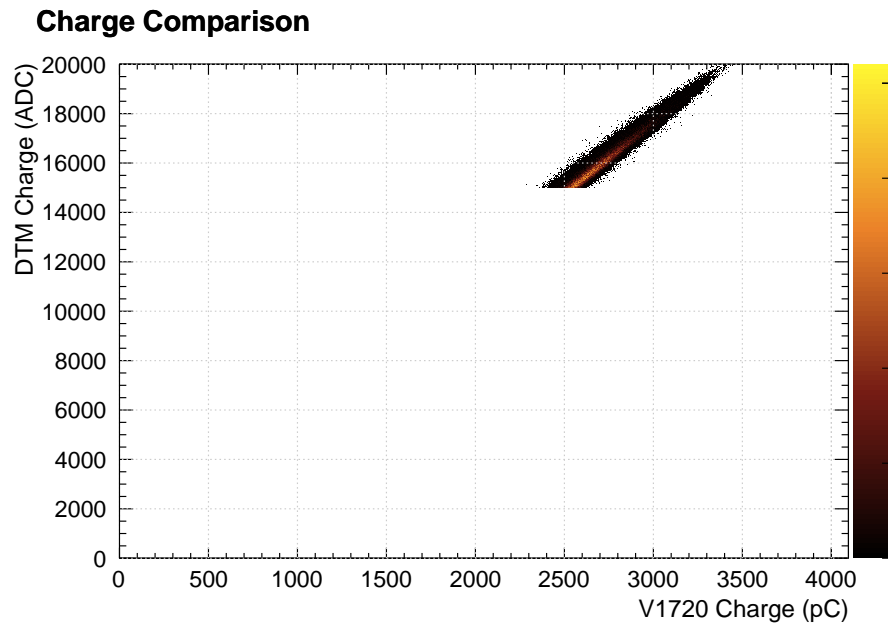
Table 5.3: Fit parameters to the charges recorded for each run type.

DTM Threshold (ADC)	Run	μ (pC)	σ (pC)
1400	304	230.9 ± 2.1e-20	12.1±1.1e-21
6000	305	1000 ± 0.035	19.8±6.2e-20
15000	306	2518 ± 0.13	30.07±0.12

5.4 Discussion

The efficiency of the trigger was found to be highly Gaussian and well fit by an error function. The total lack of outliers and partial efficiencies indicate that the trigger is working as designed. This of course does not mean that it is entirely bug-free yet; the Fprompt cut efficiency has yet to be investigated and will be done once the rate of β events become appreciable as cool down and argon filling continue.

The fit to the efficiencies decrease at the lower charge limit, the high threshold fit giving a χ^2 of ~ 0.5 where as at the low threshold this is increased to ~ 3. It is likely that this is due to the zero length encoding (ZLE) implemented in the FPGA on each of the V1720 digitizers. The algorithm will cause the V1720 to only record an event if a threshold of charge is meet within a set length of time [38]. The data reduction achieved by this method is significant, however compared to the analog signal received by the DTM, there is a bias towards lower charge in the V1720s. The fractional difference of this grows at lower energy giving a higher efficiency at that charge than expected, skewing the low end of the efficiency plots. Although the ZLE limit is set to only 2 pC for each PMT, the total of 255 signals can cause significant bias at low energies. It is of interest for future work to investigate this effect of the ZLE charge threshold on the low charge efficiency.

The efficiency has a steep turn on region even at high temperature without any irregularities at all beyond those discussed above. As the PSD done in the trigger is course, the characteristic shape is well enough described by an erf with the fit parameters given in Table 5.3. The finer scale PSD in the back end won't have the ZLE issue as the counting

of individual photons, instead of the total PMT signal, will eliminate the issue. The steep and well defined turn on region will allow for excellent PSD in the detector.

Chapter 6

Summary & Conclusions

DEAP-3600 is currently undergoing the final stages of argon filling and cooling. The detector is projected to take first data as early as Summer 2016. A functioning trigger capable of reducing the high natural β background in atmospheric argon has been developed, debugged, and shown to function as designed. The efficiency and operation of the trigger has been studied and found to be well characterized by a Gaussian error function allowing accurate uncertainty calculations once data cuts are made.

Slight divergence from a Gaussian model of the trigger threshold have been observed at low energy. It is expected however, that the large PSD separation between the background events and the WIMP region of interest will mean this slight shift to higher efficiency will not affect the mitigation of unwanted backgrounds as a large safety factor can be introduced. The final threshold definitions will take into account the relation between detector downtime due to the system latency while recording events and the probability of miscategorizing a non-β event following the fit efficiency erf. A good separation in the Fprompt and charge of these events will allow this uncertainty to be minimized, maximizing the detectors sensitivity.

6.1   Future Work

A new clock distribution system which will improve timing issues in the data acquisition system has been developed. The DTM with the new clock distribution has yet to be thoroughly tested and will need to be studied in the same manner as this study follows for the current trigger. Although no functional change is expected in the trigger itself, this has not yet been shown. Future work will go into ensuring the correct operation and stability of the system.

Additional development of the trigger may be necessary, such as protection against buffer overflow in the case of high rates. Trigger development and improvements will continue as needed but the currently installed trigger is functioning. It is also necessary to calibrate the energy and Fprompt levels for proper event selection which will be done once the rate of β events in the detector become appreciable as argon is added. A similar study to the energy thresholds must be done for the Fprompt thresholds. The efficiency erf fits will be used as possible sources of detection uncertainty once these thresholds are defined.

Bibliography

[1]   Abbasi et. al. "Multiyear search for dark matter annihilations in the Sun with the AMANDA-II and IceCube detectors". In: *Phys. Rev. D* 85 (4 Feb. 2012), p. 042002.

[2]   P.-A. Amaudruz et al. "Radon backgrounds in the DEAP-1 liquid-argon-based Dark Matter detector". In: *Astroparticle Physics* 62 (2015), pp. 178–194. ISSN: 0927-6505.

[3]   ANTARES Collaboration. "First results on dark matter annihilation in the Sun using the ANTARES neutrino telescope". In: *jcap* 11, 032 (Nov. 2013), p. 032. arXiv: 1302.6516 [astro-ph.HE].

[4]   E. Aprile et al. "Dark Matter Results from 225 Live Days of XENON100 Data". In: *Physical Review Letters* 109.18, 181301 (Nov. 2012), p. 181301. arXiv: 1207.5988 [astro-ph.CO].

[5]   R. Barrena et al. "The dynamical status of the cluster of galaxies 1E0657-56". In: *aap* 386 (May 2002), pp. 816–828.

[6]   K. G. Begeman, A. H. Broeils, and R. H. Sanders. "Extended rotation curves of spiral galaxies: dark haloes and modified dynamics". In: *Monthly Notices of the Royal Astronomical Society* 249.3 (1991), pp. 523–537.

[7]   Gianfranco Bertone, Dan Hooper, and Joseph Silk. "Particle dark matter: evidence, candidates and constraints". In: *Physics Reports* 405.5-6 (2005), pp. 279–390.

[8]   M G Boulay and the Deap Collaboration. "DEAP-3600 Dark Matter Search at SNO-LAB". In: *Journal of Physics: Conference Series* 375.1 (2012), p. 012027.

[9] M. G. Boulay and A. Hime. "Direct WIMP Detection Using Scintillation Time Discrimination in Liquid Argon". In: *ArXiv Astrophysics e-prints* (Nov. 2004). eprint: `astro-ph/0411358`.

[10] M. G. Boulay et al. "Measurement of the scintillation time spectra and pulse-shape discrimination of low-energy beta and nuclear recoils in liquid argon with DEAP-1". In: *ArXiv e-prints* (Apr. 2009). arXiv: `0904.2930 [astro-ph.IM]`.

[11] Rene Brun and Fons Rademakers. "ROOT - An object oriented data analysis framework". In: *Nuclear Instruments and Methods in Physics Research Section A: Accelerators, Spectrometers, Detectors and Associated Equipment* 389.1-2 (1997). New Computing Techniques in Physics Research V, pp. 81–86. ISSN: 0168-9002. DOI: `http://dx.doi.org/10.1016/S0168-9002(97)00048-X`.

[12] Alistair Butcher. "SEARCHING FOR DARK MATTER WITH DEAP-3600". PhD. University of London, Sept. 2015.

[13] *CAEN Upgrader. Firmware Upgrade Tool for Front-end Boards Bridges and VME Power Supply.* titleaddon. Guide 2512. May 2014.

[14] D Casadei. "Estimating the selection efficiency". In: *Journal of Instrumentation* 7.08 (2012), P08021.

[15] Douglas Clowe, Anthony Gonzalez, and Maxim Markevitch. "Weak-Lensing Mass Reconstruction of the Interacting Cluster 1E 0657-558: Direct Evidence for the Existence of Dark Matter". In: *The Astrophysical Journal* 604.2 (2004), p. 596.

[16] DEAP-3600 Collaboration. "The DEAP-3600 Dark Matter Experiment". Feb. 2016.

[17] W. de Boer et al. "EGRET excess of diffuse galactic gamma rays as tracer of dark matter". In: *aap* 444 (Dec. 2005), pp. 51–67. eprint: `astro-ph/0508617`.

[18] DEAP Collaboration et al. "DEAP-3600 Dark Matter Search". In: *ArXiv e-prints* (Oct. 2014). arXiv: `1410.7673 [physics.ins-det]`.

[19] Tadayoshi Doke et al. "Let dependence of scintillation yields in liquid argon". In: *Nuclear Instruments and Methods in Physics Research Section A: Accelerators, Spectrometers, Detectors and Associated Equipment* 269.1 (1988), pp. 291–296. ISSN: 0168-9002.

[20] F. Donato et al. "Constraints on WIMP Dark Matter from the High Energy PAMELA Data". In: *Phys. Rev. Lett.* 102 (7 Feb. 2009), p. 071301.

[21] Toby Falk, Keith A. Olive, and Mark Srednicki. "Heavy sneutrinos as dark matter". In: *Physics Letters B* 339.3 (1994), pp. 248–251. ISSN: 0370-2693.

[22] K. C. Freeman. "On the Disks of Spiral and so Galaxies". In: *apj* 160 (June 1970), p. 811.

[23] G. Hinshaw et al. "Nine-year Wilkinson Microwave Anisotropy Probe (WMAP) Observations: Cosmological Parameter Results". In: *The Astrophysical Journal Supplement Series* 208.2 (2013), p. 19.

[24] A. Hitachi et al. "Effect of ionization density on the time dependence of luminescence from liquid argon and xenon". In: *prb* 27 (May 1983), pp. 5279–5285.

[25] Gerard Jungman, Marc Kamionkowski, and Kim Griest. "Supersymmetric dark matter". In: *Physics Reports* 267.5 (1996), pp. 195–373.

[26] Theodor Kaluza. "Zum unitatsproblem der physik". In: *Sitzungsber. Preuss. Akad. Wiss. Berlin.(Math. Phys.)* 1921.966972 (1921), p. 45.

[27] J. C. Kapteyn. "First Attempt at a Theory of the Arrangement and Motion of the Sidereal System". In: *apj* 55 (May 1922), p. 302.

[28] Oskar Klein. "Quantentheorie und funfdimensionale Relativitatstheorie". In: *Zeitschrift fur Physik* 37.12 (Dec. 1926), pp. 895–906. ISSN: 0044-3328.

[29] D.R. Lide. *CRC Handbook of Chemistry and Physics: A Ready-reference Book of Chemical and Physical Data.* CRC-Press, 1995. ISBN: 9780849305955.

[30] W. H. Lippincott et al. "Scintillation time dependence and pulse shape discrimination in liquid argon". In: *prc* 78.3, 035801 (Sept. 2008), p. 035801. arXiv: `0801.1531` `[nucl-ex]`.

[31] LUX Collaboration et al. "Improved WIMP scattering limits from the LUX experiment". In: *ArXiv e-prints* (Dec. 2015). arXiv: `1512.03506`.

[32] M. Milgrom. "A modification of the Newtonian dynamics as a possible alternative to the hidden mass hypothesis". In: *apj* 270 (July 1983), pp. 365–370.

[33] Mordehai Milgrom and Robert H. Sanders. "Modified Newtonian Dynamics and the "Dearth of Dark Matter in Ordinary Elliptical Galaxies"". In: *The Astrophysical Journal Letters* 599.1 (2003), p. L25.

[34] Robert S. Mulliken. "Potential Curves of Diatomic Rare-Gas Molecules and Their Ions, with Particular Reference to Xe2". In: *The Journal of Chemical Physics* 52.10 (1970), pp. 5170–5180. DOI: `http://dx.doi.org/10.1063/1.1672756`.

[35] H. Murayama. "Supersymmetry Phenomenology". In: *Particle Physics*. Ed. by G. Senjanovic and A. Y. Smirnov. 2000, p. 296. eprint: `hep-ph/0002232`.

[36] Marc Paterno. *Calculating efficiencies and their uncertainties*. Tech. rep. United States. Department of Energy, 2004.

[37] Tina Pollmann. "Alpha backgrounds in the DEAP Dark Matter search experiment". PhD. Queens University, Aug. 2012.

[38] F. Retiere et al. "DEAP trigger and readout electronics". In: *Nuclear Science Symposium and Medical Imaging Conference (NSS/MIC), 2012 IEEE*. Oct. 2012, pp. 1802–1805. DOI: `10.1109/NSSMIC.2012.6551421`.

[39] M. S. Roberts and A. H. Rots. "Comparison of Rotation Curves of Different Galaxy Types". In: *aap* 26 (Aug. 1973), pp. 483–485.

[40] V. C. Rubin and W. K. Ford Jr. "Rotation of the Andromeda Nebula from a Spectroscopic Survey of Emission Regions". In: *apj* 159 (Feb. 1970), p. 379.

[41] V. C. Rubin, W. K. Ford Jr., and S. D'Odorico. "Emission-Line Intensities and Radial Velocities in the Interacting Galaxies NGC 4038-4039". In: *apj* 160 (June 1970), p. 801.

[42]   R. W. Schnee. "Introduction to Dark Matter Experiments". In: *Physics of the Large and the Small: TASI 2009*. Ed. by C. Csaki and S. Dodelson. Mar. 2011, pp. 775–829. arXiv: `1101.5205 [astro-ph.CO]`.

[43]   Y. Sofue. "Mass Distribution and Rotation Curve in the Galaxy". In: *Planets, Stars and Stellar Systems. Volume 5: Galactic Structure and Stellar Populations*. Ed. by T. D. Oswalt and G. Gilmore. 2013, p. 985.

[44]   Felix Stoehr et al. "Dark matter annihilation in the halo of the Milky Way". In: *Monthly Notices of the Royal Astronomical Society* 345.4 (2003), pp. 1313–1322.

[45]   N. Thonnard and G. S. Hurst. "Time-Dependent Study of Vacuum-Ultraviolet Emission in Argon". In: *Phys. Rev. A* 5 (3 Mar. 1972), pp. 1110–1121.

[46]   Jian Wang. "QCD Higher-Order Effects and Search for New Physics". In: Berlin, Heidelberg: Springer Berlin Heidelberg, 2016. Chap. Introduction to the Standard Model of Particle Physics, pp. 1–10. ISBN: 978-3-662-48673-3.

[47]   F. Zwicky. "Die Rotverschiebung von extragalaktischen Nebeln". In: *Helvetica Physica Acta* 6 (1933), pp. 110–127.

[48]   F. Zwicky. "The redshift of extragalactic nebulae". In: *Helv. Phys. Acta* 6 (1933), p. 110.